Available online at www.sciencedirect.com

SCIENCE DIRECT®

ELSEVIER

Journal of Sound and Vibration 288 (2005) 133–176

JOURNAL OF SOUND AND VIBRATION

www.elsevier.com/locate/jsvi

A numerical simulation of the hole-tone feedback cycle based on an axisymmetric discrete vortex method and Curle's equation

M.A. Langthjem*, M. Nakano

Department of Mechanical Systems Engineering, Faculty of Engineering, Yamagata University,
4-3-16 Jonan, Yonezawa, Yamagata 992-8510, Japan

Received 12 November 2003; received in revised form 29 March 2004; accepted 20 December 2004
Available online 14 March 2005

Abstract

An axisymmetric numerical simulation approach to the hole-tone self-sustained oscillation problem is developed, based on the discrete vortex method for the incompressible flow field, and a representation of flow noise sources on an acoustically compact impingement plate by Curle's equation. The shear layer of the jet is represented by 'free' discrete vortex rings, and the jet nozzle and the end plate by bound vortex rings. A vortex ring is released from the nozzle at each time step in the simulation. The newly released vortex rings are disturbed by acoustic feedback. It is found that the basic feedback cycle works hydrodynamically. The effect of the acoustic feedback is to suppress the broadband noise and reinforce the characteristic frequency and its higher harmonics. An experimental investigation is also described. A hot wire probe was used to measure velocity fluctuations in the shear layer, and a microphone to measure acoustic pressure fluctuations. Comparisons between simulated and experimental results show quantitative agreement with respect to both frequency and amplitude of the shear layer velocity fluctuations. As to acoustic pressure fluctuations, there is quantitative agreement w.r.t. frequencies, and reasonable qualitative agreement w.r.t. peaks of the characteristic frequency and its higher harmonics. Both simulated and measured frequencies f follow the criterion $L/u_c + L/c_0 = n/f$ where L is the gap length between nozzle

---

*Corresponding author. Tel.: +81 238 26 3326; fax: +81 238 26 3205.
E-mail addresses: mikael@yz.yamagata-u.ac.jp (M.A. Langthjem), nakano@mnaka.yz.yamagata-u.ac.jp (M. Nakano).

doi:10.1016/j.jsv.2004.12.023

Nomenclature

A_d	amplitude of forced excitations, see Eq. (53)
$\mathscr{A}_n$	ring area used in the computation of the monopole acoustic pressure, see Eq. (42)
c_0	speed of sound
d_0	diameter of nozzle and hole in end plate
D_n	distance from the point of observation to the *n*th ring force, see Eq. (39)
E	complete elliptic integral of second kind, defined by Eq. (4)
f	characteristic hole-tone frequency
f_d	forcing frequency
$f_{\max}$	Nyquist frequency
$\mathbf{f}_n$	force vector with components (f_{xn}, f_{rn})
G	Green's function, see Eq. (31)
$H(s)$	the Heaviside unit function, which is zero for $s<0$ and unity for $s>0$
$H_0^{(1)}$	Hankel function of first kind and zeroth order
HPL	hydrodynamic pressure level
i	complex unit, $\sqrt{-1}$
J_m	Bessel function of *m*th order
k	acoustic wavenumber, ω/c_0
K	complete elliptic integral of first kind, defined by Eq. (4)
L	length of the gap between nozzle exit and end plate
$\mathbf{n}$, n	normal vector
p	pressure in the (t, x, r)-domain
P	pressure in the (ω, x, r)-domain
$\mathscr{P}$	pressure in the (ω, ζ, r)-domain
r	radius in the axisymmetric cylinder coordinate system (x, r)
R_n	radial distance between the point of observation and the *n*th ring force
SPL	sound pressure level
t	time
$u_{x\pm}$	slip velocity above (+) and below (−) the nozzle edge
$\mathbf{u} = (u_x, u_r)$	hydrodynamic velocity (of the incompressible 'background flow')
$\mathbf{v} = (v_x, v_r)$	acoustic perturbation velocity
VFL	velocity fluctuation level
x	axial coordinate in the axisymmetric cylinder coordinate system (x, r)
x_e	axial position of the nozzle exit
x_s	axial position of the end plate
X	axial distance between point of observation and end plate
γ	strength of vortex sheet
Γ	strength of vortex ring
$\delta(x)$	the usual (Dirac) delta function, defined such that $\int_{-\infty}^{\infty} \mathscr{F}(x)\delta(x - x_*)\,\mathrm{d}x = \mathscr{F}(x_*)$
$\delta(r)/\pi r$	the axisymmetric delta function, defined such that $\int_0^{\infty} \mathscr{F}(r)\delta(r - r_*)\,\mathrm{d}r = \frac{1}{2}\mathscr{F}(r_*)$
ε	vortex ring smoothing parameter
ρ_0	fluid density
σ	complex function defined by Eq. (38)
τ_n	retarded time given by $t - D_n/c_0$
ζ	axial coordinate in the Fourier-transformed domain
Φ_n	velocity potential defined by Eq. (34)
ψ	acoustic perturbation velocity potential defined by Eq. (43)
Ψ	stream function for vortex ring, defined by Eq. (3)
ω	angular velocity
Ω	vorticity
$\tilde{\bullet}$	the Fourier transform of $\bullet$
$[\ ]_{\tau_n}$	expression inside [ ] to be evaluated at the retarded time $\tau_n = t - D_n/c_0$

exit and end plate, u_c is the shear layer convection velocity, c_0 is the speed of sound, and n is a mode number ($n = \frac{1}{2}, 1, \frac{3}{2}, \ldots$). The experimental results however display a complicated pattern of mode jumps, which the numerical method cannot capture.

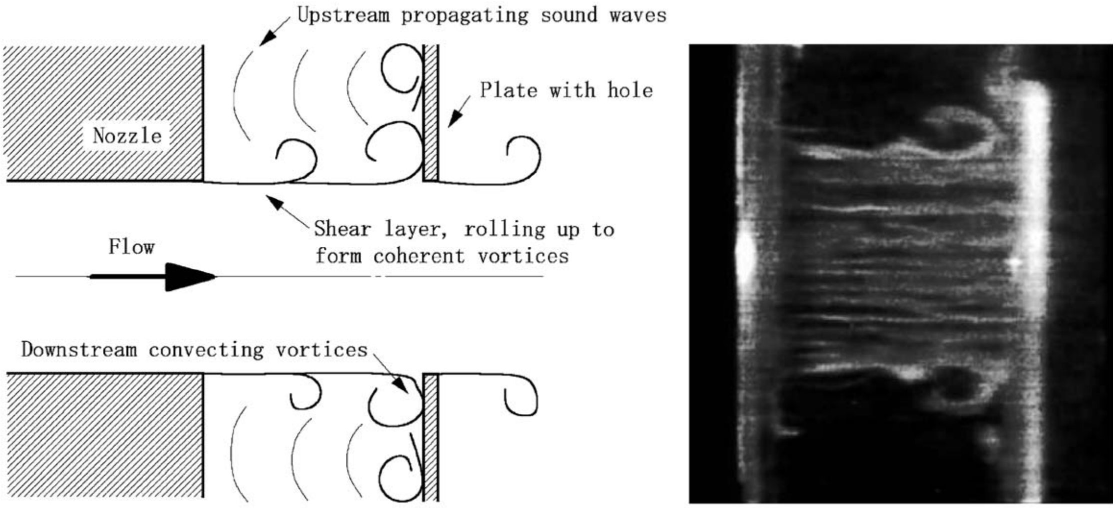

(a) (b)

Fig. 1. (a) Geometry and physical features of the hole-tone problem. (b) Flow visualization of the vortex roll-up.

1. Introduction

The sound produced when a jet, issued from a circular nozzle or a hole in a plate, goes through a second plate with a hole of the same diameter as the jet is referred to as the hole-tone. The geometry of the problem is sketched in Fig. 1, which also shows the principal physical features. It is widely accepted that the responsible mechanism is shear layer instability, and that the characteristic, discrete tone is maintained by an acoustic feedback mechanism. This was suggested already in 1896 by Rayleigh [1] (referring to the system as the 'bird-call'), who explained the basic mechanism as follows: 'When a symmetrical excrescence [vortex ring][1] reaches the second plate, it is unable to pass the hole with freedom, and the disturbance is thrown back, probably with the velocity of sound, to the first plate, where it gives rise to a further disturbance, to grow in its turn during the progress of the jet.'

Rayleigh also pointed out that the disturbances are axisymmetric (varicose). Later experiments [2] verified this,[2] and that the shear layer periodically rolls up into big, distinct vortex rings ('smoke rings'). It was furthermore found that the oscillations, caused by the impingement of these vortex rings onto the end plate, occur in specific stages of approximately constant Strouhal number $St = \text{(frequency)} \times \text{(gap length)}/\text{(average jet speed)}$, and that transference from one stage to another is associated with hysteresis. In other words, the tone experiences jumps in the frequency by increasing jet velocity, and the jumps back occur at other values when the velocity is again decreased.

---

[1] Added by the authors.

[2] Chanaud and Powell [2] wrote that, 'The disturbances were found to be unambiguously symmetrical, as observed by other investigators.'

Lighthill [3] argued that acoustic sources in a flowing fluid can be represented by monopoles (associated with fluctuating volume sources), dipoles (associated with fluctuating surface forces), and quadrupoles (associated with turbulent velocity fluctuations). In this pioneering work Lighthill was mainly interested in the noise generation by turbulence in a free field. Curle [4] extended Lighthill's theory to show that the sound field from flow incident upon solid boundaries can be represented by a surface distribution of dipoles. Powell [5] showed, by considering an image system, that for an incident inviscid fluid the pressure dipole distribution on a plane, infinite and rigid surface cancels out such that the effect of the surface is to account for the reflection of quadrupoles only. Ffowcs Williams and Hawkings [6] generalized the work of Lighthill and Curle to account for surfaces in arbitrary motion.

If U is a characteristic flow speed the intensity and power output in the far field (far away from the (compact) noise sources) varies as U^4 for a monopole, as U^6 for a dipole, and as U^8 for a quadrupole. For low-speed flows (small Mach number) the monopole is thus an efficient sound source; a quadrupole is a very inefficient one.

Hole-tone experiments with low-speed jets [2] have indicated that the sound generated at the end plate is mainly of monopole type if the hole diameter is much smaller, and the end plate diameter much larger, than the acoustic wavelength $\lambda = (\text{speed of sound})/(\text{frequency})$. In this case the hole is acoustically compact; the plate is not. On the other hand, the sound is mainly of dipole type if the end plate is small ('ring-like') [7]. The monopole effect is due to the unsteady volume flow through the hole. The dipole effect is due to the unsteady fluid forces on the plate.

An estimate of the characteristic (dominating/most unstable) frequency f can be obtained from the criterion (Rossiter's equation [7])

$$\frac{L}{u_c} + \frac{L}{c_0} = \frac{n}{f}, \tag{1}$$

where L is the gap length, u_c is the shear layer convection velocity, c_0 is the speed of sound, and n is the mode number which may take the values $\frac{1}{2}, 1, \frac{3}{2} \ldots$. The first term on the left-hand side represents the time it takes a vortex to travel from the nozzle exit to the end plate; the second term represents the time it takes the acoustic feedback signal to travel from the end plate and back to the nozzle exit. The right-hand side represents the period of vortex ring separation. The shear layer convection velocity u_c is typically $0.6u_0 - 0.7u_0$, where u_0 is the mean jet speed [7,11]. As to the meaning of the right-hand side, it is instructive to rewrite the equation as $L/n = u_c\{f(1 + u_c/c_0)\}$; this expresses the distance between consecutive vortices. Accordingly, in the inverse expression, n/L has the meaning of a wavenumber.

Howe [7] derived Eq. (1) from an expression for the acoustic pressure (at large distances from the jet) generated by the large vortex rings. Assuming that vortex rings only are shed from the jet nozzle at the beginning of the half-cycles where the pressure perturbations are positive, the right-hand side takes the form $(n - \frac{1}{2})/f, n = 1, 2, \ldots,$ corresponding to the non-integer values in Eq. (1). But the experimental and numerical simulation results to be presented in the following, show that both integer and non-integer values of n in Eq. (1) are possible. The integer values correspond to cases where vortex rings are shed at every half-cycle of the pressure perturbations.

Despite the long history of the hole-tone problem, a comprehensive analytical/numerical solution has not yet been given. In addition to the appeal as an unsolved classical problem, there are many practical motivations for further studies. One example is solid propellant rocket motors. The fuel is often in the form of axially segmented rings, and holed restrictor plates, which separate the fuel elements, initiate hole-tones [7–9]. Automobile intake- and exhaust-systems, ventilation systems, gas distribution systems [10], and so on, may also generate undesirable hole-tones. A better understanding of the problem may also lead to improvement of some musical wind instruments (flutes, etc.), and to the design of new types. Improved understanding may thus be rewarding for many branches of engineering.

For general surveys of hole-, ring-, and edge-tone problems, see [12,13,7]. As to mathematical models, the main focus has been on purely 2D problems, such as the edge-tone problem [14,15], and the cavity problem [7].

This paper presents an axisymmetric numerical simulation approach to the hole-tone problem, based on the discrete vortex method [16] for the unsteady jet flow, and the theory of aerodynamic noise [3] for the acoustic feedback. The discrete vortex method has previously been successfully applied to several purely 2D (plane) representations of self-sustained oscillation problems, for example a gas distribution system with closed side branches [10], plates in tandem in a duct [17], and the resonator tube [18].

Lighthill's approach [3] is based on the assumption that the acoustic field does not act back on the hydrodynamic (incompressible 'background') flow field, in contrast to the present problem. In the present paper it is suggested to model the acoustic back-reaction by applying the flow noise equation *iteratively*, to modify the background flow field in small steps. In the numerical scheme the feedback loop is modelled as follows. Hydrodynamic pressure fluctuations on the end plate generates acoustic pressure fluctuations (compression waves). The corresponding acoustic disturbance velocities acting near the nozzle exit are evaluated at each time step. These are added to the hydrodynamic velocities generated by the discrete vortex rings which represent the shear layer of the jet. As shed vortex rings proceed from the nozzle towards the end plate they roll up to emulate a big vortex. This vortex hits the end wall and creates a new hydrodynamic pressure fluctuation, which is thrown back to the nozzle exit as a new acoustic disturbance, just as in Rayleigh's explanation.

For low Mach number flows it is known that the feedback mechanism works hydrodynamically (i.e., instantaneously, without acoustic/compressibility effects), as the nozzle then lies only a fraction of the fundamental acoustic wavelength away from the end plate. This is also verified in the present work. But it is still interesting to consider modifications due to acoustic back-reaction on the flow, even though these are small. There is a monopole sound field due to the unsteady flow through the hole in the end plate. But in the case considered the end plate diameter is relatively small (5 × the jet/hole diameter and 0.15 × the typical acoustic wavelength) and the pressure fluctuations due to the passage of the big vortex rings over the outer edge generates a much more powerful dipole sound field. The corresponding acoustic feedback signal reinforces the characteristic hole-tone frequency component and its higher harmonics. In this sense the acoustic feedback mechanism can be said to provide a 'compressibility correction' to the governing background flow.

Interaction between the background flow field and the acoustic field is included in two of the above-mentioned discrete vortex method-based self-sustained oscillation problems [17,18]. In these studies the whole acoustic field is determined in the frequency domain, numerically by application of the finite element method in Ref. [17] and by a conformal mapping method in

Ref. [18]. The first of these approaches would be very computationally demanding for the present problem. The second approach works only for plane problems.

The plan of the paper is as follows. In Section 2 the discrete vortex model of the unstable jet flow is discussed. Expressions for the acoustic pressure fluctuations are derived in Section 3, using the differential form of Curle's equation as start-point. Expressions for the acoustic feedback velocities are derived in closed form in Section 4. A mechanism for forced acoustic excitation is discussed briefly in Section 5. Section 6 discusses computational aspects of the problem. Numerical results are presented and discussed in Section 7. Section 8 describes experiments and compares experimental and computational results. Finally, in Section 9, the results are discussed and some conclusions are drawn. The paper also includes three appendices, concerned with specific mathematical details.

2. Basic jet flow

2.1. Vortex ring theory

An axisymmetric jet of radius $r = r_0$ is discharging from a nozzle at the position $x = x_e$ in the axisymmetric cylindrical polar coordinate system (x, r). The shear layer of the jet is impinging upon the edge of a circular hole (aperture), also of radius r_0, in a parallel plate of radius r_{plate}, placed at $x = x_s = x_e + L$.

The shear layers of the jets issued from the nozzle and from the end plate hole are first thought to be represented by continuous vortex sheets, and the nozzle and end plate by bound vortex sheets. These vortex sheets are then discritized (lumped) into necklaces of discrete vortex rings. The present method is thus based on the 'usual' discrete vortex method which considers a vortex sheet as lumped into 'particles' [19]. This is equivalent to the approaches of Acton [20], Dahm et al. [21], and Jing and Sun [22], but different from, and simpler than, the approaches of de Bernadinis et al. [23], Martin and Meiburg [24], and Nitsche and Krasny [25], where the smooth sheets are discretized via interpolation of the integrals over distributed vortex strength.

Nitsche and Krasny's [25] vortex ring model is used. This is a 'desingularized' version of the thin-cored circular vortex ring [26,27]. The induced velocity $\mathbf{u} = (u_x, u_r)$ at a location (x, r) from a single vortex ring, of strength Γ and located at (x_v, r_v), is obtained from

$$u_x(x, r, x_v, r_v) = \frac{1}{r}\frac{\partial \Psi}{\partial r}(x, r, x_v, r_v), \quad u_r(x, r, x_v, r_v) = -\frac{1}{r}\frac{\partial \Psi}{\partial x}(x, r, x_v, r_v), \tag{2}$$

where the stream function Ψ is given by

$$\begin{aligned} \Psi(x, r, x_v, r_v) &= \frac{\Gamma}{2\pi}(\eta_1 + \eta_2)\{K(\lambda) - E(\lambda)\}, \\ \lambda &= (\eta_2 - \eta_1)/(\eta_2 + \eta_1), \\ \eta_1 &= \{(x - x_v)^2 + (r - r_v)^2 + \varepsilon^2\}^{1/2}, \\ \eta_2 &= \{(x - x_v)^2 + (r + r_v)^2 + \varepsilon^2\}^{1/2}. \end{aligned} \tag{3}$$

Here $K(\lambda)$ and $E(\lambda)$ are the complete elliptic integrals of first and second kind, respectively, defined by [28]

$$K(\lambda)=\int_0^{\pi/2}(1-\lambda^2\sin^2\theta)^{-1/2}\,\mathrm{d}\theta,\quad E(\lambda)=\int_0^{\pi/2}(1-\lambda^2\sin^2\theta)^{1/2}\,\mathrm{d}\theta. \tag{4}$$

These functions are evaluated numerically by using Carlson's algorithms [29]. Analytical evaluation of the derivatives in Eq. (2) is, for completeness, shown in Appendix A.

The parameter ε in the η_1 and η_2 functions is a smoothing, or regularization, parameter, corresponding in effect to a finite vortex sheet thickness. It is also called a vortex-blob regularization [30]. [Considering the 2D case, a vortex-blob has a core of finite size, contrary to a point-vortex.] It may also be thought of as 'artificial viscosity'. Tryggvason et al. [31] explain, in a study on roll-up of a 2D vortex sheet, that, 'it may...not be possible to identify a physically meaningful role for fixed values of a regularization parameter', but argue that $\varepsilon>0$ works as viscosity, as the vorticity field is non-zero away from the vortex sheet. It will be illustrated in Section 7 that $\varepsilon>0$ also 'smears out' the vorticity in the present problem.

On the axis $r=0$ the induced velocity is

$$u_x(x,0,x_v,r_v)=\frac{\Gamma}{2}\frac{r_v^2}{\{(x-x_v)^2+r_v^2+\varepsilon^2\}^{3/2}},\quad u_r(x,0,x_v,r_v)=0. \tag{5}$$

The (azimuthal) vorticity is

$$\Omega=\frac{\partial u_r}{\partial x}-\frac{\partial u_x}{\partial r}=-\frac{1}{r}\frac{\partial^2\Psi}{\partial x^2}-\frac{\partial}{\partial r}\left(\frac{1}{r}\frac{\partial\Psi}{\partial r}\right). \tag{6}$$

The evaluation of this quantity (for $r>0$) is also given in Appendix A. Eq. (5) gives that $\Omega=0$ on the axis $r=0$.

2.2. Representation of solid surfaces

The surface of the exit pipe is represented by N_{pipe} vortex rings, placed equidistantly at the positions $(x_j^{\circ a},r_0)$, $j=1,2,\ldots,N_{\text{pipe}}$. Control points are placed at (x_j^{*a},r_0), $j=1,2,\ldots,N_{\text{pipe}}-1$, midway between these vortices. The mean jet flow is provided by N_{ev} vortex rings placed on the upstream end of the exit pipe, at the equidistant positions $(x_0,r_j^{\circ b})$, $j=1,2,\ldots,N_{ev}$. The radii $r_j^{\circ b}$ of these rings are placed in between $N_{ev}+1$ control points, located at (x_0,r_j^{*b}), $j=1,2,\ldots,N_{ev}+1$. Similar to the exit pipe, the end plate is represented by N_{plate} concentric vortex rings, placed equidistantly at the positions $(x_s,r_j^{\circ c})$, $j=1,2,\ldots,N_{\text{plate}}$, with the control points (x_s,r_j^{*c}), $j=1,2,\ldots,N_{\text{plate}}-1$, placed in between. A diagram of the system is shown in Fig. 2.

The strengths Γ_j^{bound} of the bound vortex rings are determined from the following conditions:

1. The r-composant u_r of the velocity is zero on the surface of the exit pipe;
2. The (axial) velocity distribution of the mean flow-providing upstream end of the exit pipe end is uniform;
3. The x-composant u_x of the velocity is zero on the surface of the end plate;

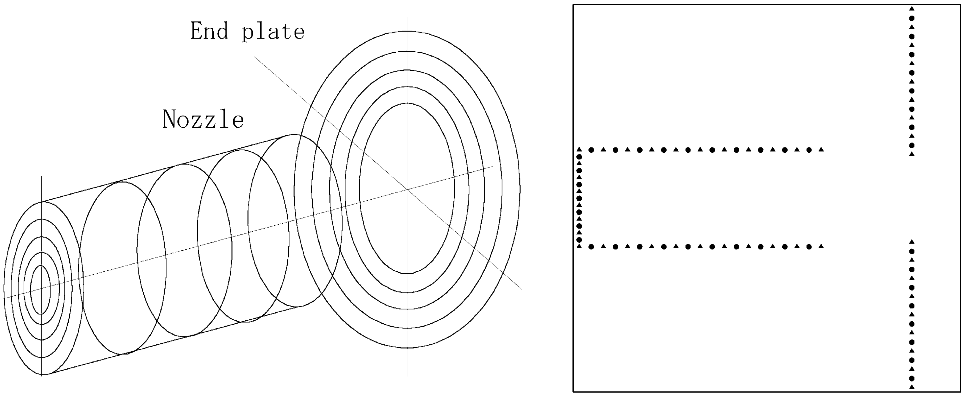

(a) (b)

Fig. 2. (a) Schematic diagram showing the distribution of bound vortex rings on the nozzle and the end plate. (b) A cut through the cylinder axis. Triangles indicate vortex rings and dots indicate control points.

4. The axial velocity u_x at $r = 0$ must be equal to the mean jet speed u_0 a little distance $\hat{\varepsilon}$ downstream from the nozzle exit $(x_e + \hat{\varepsilon})$, and a little distance upstream from the end plate $(x_s - \hat{\varepsilon})$.

The velocity at some position (x, r) is obtained as the sum of the induced velocities from the bound and the free vortices. Let N_Σ denote the sum of the N_{bound} bound and N_{free} free vortices. The four physical conditions above can then be expressed mathematically as

$$
\begin{aligned}
&\sum_{i=1}^{N_\Sigma} u_r(x_j^{*a}, r_0, x_i, r_i) = 0, \quad j = 1, 2, \ldots, N_{\text{pipe}} - 1,\\
&\sum_{i=1}^{N_\Sigma} \{u_x(x_0, r_j^{*b}, x_i, r_i) - u_x(x_0, r_{j+1}^{*b}, x_i, r_i)\} = 0, \quad j = 1, 2, \ldots, N_{ev},\\
&\sum_{i=1}^{N_\Sigma} u_x(x_s, r_j^{*c}, x_i, r_i) = 0, \quad j = 1, 2, \ldots, N_{\text{plate}} - 1,\\
&\sum_{i=1}^{N_\Sigma} u_x(x_e + \hat{\varepsilon}, 0, x_i, r_i) = u_0; \quad \sum_{i=1}^{N_\Sigma} u_x(x_s - \hat{\varepsilon}, 0, x_i, r_i) = u_0,
\end{aligned}
\tag{7}
$$

which is a system of $N_{\text{bound}} = N_{\text{pipe}} + N_{\text{plate}} + N_{ev}$ equations for determining the same number of unknown vortex strengths $\mathbf{\Gamma}^{\text{bound}} = \{\Gamma_1^{\text{bound}}, \ldots, \Gamma_{N_{\text{bound}}}^{\text{bound}}\}^{\mathrm{T}}$. The matrix equation system corresponding to Eq. (7) takes the form

$$
\mathbf{A}\mathbf{\Gamma}^{\text{bound}} = \mathbf{b}. \tag{8}
$$

Here the $N_{\text{bound}} \times N_{\text{bound}}$ matrix $\mathbf{A}$ contains functions (combinations in accordance with Eq. (7)) of the influence coefficients $\partial \mathbf{u}(x_i, r_i, x_j, r_j)/\partial \Gamma_j$. The vector $\mathbf{b}$ contains the velocity contributions from the free vortices, i.e.,

$$b_j = -\sum_{i=1}^{N_{\text{free}}} \mathscr{F}\{\mathbf{u}(x_j, r_j, x_i, r_i)\}, \tag{9}$$

where $\mathscr{F}\{\}$ symbolizes the four successive 'operators' defined in Eq. (7). It is noted that for bound vortices (i.e., in the matrix **A**) the smoothing parameter ε in Eq. (3) is set equal to zero, as values larger than zero will imply non-convergence of the solution by mesh-refinement [25]. The impingement of vortex rings with $\varepsilon > 0$ onto the end plate, represented by bound rings with $\varepsilon = 0$, does not cause any numerical problems; this will be clear from the numerical examples in Section 7.

2.3. Vortex-shedding mechanism

The rate of (continuous) shedding of circulation γ from the nozzle is governed by

$$\frac{\mathrm{d}\gamma}{\mathrm{d}t} = \tfrac{1}{2}(u_{x-}^2 - u_{x+}^2), \tag{10}$$

where t is the time, u_{x+} is the axial 'slip' velocity a little 'above' the nozzle edge, outside the tube, and u_{x-} is the velocity a little 'below', inside the tube. This equation can be obtained by integrating the tangential component of the Euler equations over the tube surface, and using the Kutta condition, which demands that the pressure a little above the nozzle edge equals the pressure a little below [16].

The vortex sheet is, at the nozzle edge (x_e, r_0), convected downstream with the average slip velocity

$$u_{xe} = \tfrac{1}{2}(u_{x+} + u_{x-}). \tag{11}$$

The slip velocities are related to the sheet strength γ_e at the edge (x_e, r_0) by the relation

$$\gamma_e = u_{x-} - u_{x+} \tag{12}$$

(e.g., [16, p. 109]). Eq. (10) can then be written as

$$\frac{\mathrm{d}\gamma}{\mathrm{d}t} = \gamma_e u_{xe}. \tag{13}$$

Eqs. (11) and (12) give the relations

$$u_{x-} = u_{xe} + \tfrac{1}{2}\gamma_e, \quad u_{x+} = u_{xe} - \tfrac{1}{2}\gamma_e. \tag{14}$$

The vortex sheet is now discretized into a 'necklace' of discrete vortex rings. The shedding is simulated as follows.

1. The strengths of the bound vortex rings are determined from the equation system (8).
2. Using Eq. (14), the slip velocities u_{x+}, u_{x-} are determined as

$$u_{x-} = u_{xe} + \tfrac{1}{2}\Gamma_e^{\text{bound}}/\ell_e, \quad u_{x+} = u_{xe} - \tfrac{1}{2}\Gamma_e^{\text{bound}}/\ell_e. \tag{15}$$

Here Γ_e^{bound} is the strength of the vortex ring placed at the edge, and ℓ_e is the distance between the edge vortex ring and the neighboring ring in upstream direction. u_{xe} is taken as the velocity at the most downstream control point. With Γ_e^{bound} being positive, $u_{x-} > u_{x+}$, and the vortex ring will, as it moves in the positive x-direction, rotate as if it rolled along the inner surface of a tube.

3. A vortex ring is released from the edge and placed at

$$x_{\text{new}} = x_e + \frac{\Delta t}{2}(u_{x+} + u_{x-}), \quad r_{\text{new}} = r_0, \tag{16}$$

and it is given the strength

$$\Gamma^{\text{free}}_{N_{\text{free}}} = \Delta t \tfrac{1}{2}(u^2_{x-} - u^2_{x+}). \tag{17}$$

Once released, the ring keeps this strength throughout the simulation, that is,

$$\frac{\mathrm{d}\Gamma^{\text{free}}_j}{\mathrm{d}t} = 0, \quad j = 1, \ldots, N_{\text{free}}, \tag{18}$$

which is known as Kelvin's theorem [19,27].

4. The positions (x_i, r_i) of all previously shed vortex rings are updated by solving the system of ordinary differential equations

$$\frac{\mathrm{d}x_i}{\mathrm{d}t} = \sum_{j=1}^{N_\Sigma} u_x(x_i, r_i, x_j, r_j), \quad \frac{\mathrm{d}r_i}{\mathrm{d}t} = \sum_{j=1}^{N_\Sigma} u_r(x_i, r_i, x_j, r_j), \quad i = 1, \ldots, N_{\text{free}}, \tag{19}$$

by means of the fourth-order Runge–Kutta scheme.[3]

5. The time is updated; $t := t + \Delta t$. If $t < t_{\max}$, return to Point 1.

If included, the vortex shedding from the outer edge and from the edge of the hole in the second plate is treated analogously to the shedding from the tube edge, and new expressions for the end plate equivalent to Eqs. (16) and (17) are added to points 3 in the algorithm above. But at the edge of the hole u_{x+} or u_{x-} may become negative. This indicates a non-separating, backward running flow on the corresponding side of the edge, and the Kutta condition will not be satisfied. Thus, if either u_{x+} or u_{x-} is less than zero, the value is *set* to zero, in order not to interfere the shedding process. The positions of the vortex rings shed from the end plate are just updated according to the first-order Euler scheme.

3. Acoustic pressure fluctuations

3.1. Statement of the problem

Let $\mathbf{x} = (x_1, x_2, x_3)$ be a point in space in rectangular coordinates (used for the time being), and let the equation $s(\mathbf{x}) = 0$ define the rigid surface of the end plate shown in Fig. 1, such that $s(\mathbf{x}) < 0$ if $\mathbf{x}$ is within the solid surface and $s(\mathbf{x}) > 0$ if $\mathbf{x}$ is in the fluid. Let the fluid velocity field be given by (u_1, u_2, u_3). By making use of the Heaviside unit function $H(s)$, which takes the value 1 if $s(\mathbf{x}) > 0$ and the value 0 if $s(\mathbf{x}) < 0$, the differential form of Curle's equation [4]

---

[3] The first-order Euler scheme is also used in some cases, to investigate the influence of updating accuracy. When used, this is explicitly stated.

can be written as [32]

$$\left(\frac{1}{c_0^2}\frac{\partial^2}{\partial t^2}-\nabla^2\right)[Hp]=\frac{\partial^2(HT_{ij})}{\partial x_i\partial x_j}-\frac{\partial}{\partial x_i}\left(f_{ij}\frac{\partial H}{\partial x_j}\right)+\frac{\partial}{\partial t}\left(\rho_0 u_j\frac{\partial H}{\partial x_j}\right), \tag{20}$$

where the (Einstein) tensor summation convention is to be applied. On the left-hand side, p is the acoustic pressure, t is the time, c_0 is the speed of sound, and ∇^2 is the Laplace operator. On the right-hand side, T_{ij} is the Lighthill stress tensor (accounting for turbulent fluctuations in momentum flux), and f_{ij} is a compressive stress tensor (fluid force per unit volume). The first term represents quadrupoles, the second dipoles, and the third monopoles.

It is noted that (20) is basically Lighthill's equation [3]

$$\frac{1}{c_0^2}\frac{\partial^2 p}{\partial t^2}-\nabla^2 p=\frac{\partial^2 T_{ij}}{\partial x_i\partial x_j} \tag{21}$$

with the boundary condition

$$\frac{\partial p}{\partial \mathrm{n}}=0 \tag{22}$$

implemented into the differential equation by use of the Heaviside function. Here $\partial/\partial\mathrm{n}$ denotes the derivative in the direction of the (outward pointing) normal vector $\mathbf{n}$ to the surface.

As mentioned in Section 1, experiments with hole-tone systems have shown that the sound generated at the end plate is mainly of monopole type if this plate is much larger than the characteristic acoustic wavelength, and mainly of dipole type if it is much smaller (i.e., acoustically compact). In the simulations to follow the end plate diameter d_{plate} is 250 mm (which is equal to five jet diameters). It will be found that the characteristic frequency $f \approx 200\,\mathrm{Hz}$ (which is in agreement with the experiments, see Section 8.2). The acoustic wavelength λ is then $\sim 1.7\,\mathrm{m}$, and the ratio $d_{\mathrm{plate}}/\lambda \approx 0.15$, which is not large. It is then assumed reasonable to consider the plate being acoustically compact.

The typical (reference) jet speed is 10 m/s. With a sound speed of 340 m/s the Mach number is ~ 0.03 which is very small. The quadrupole sources (in the model due to interaction of the discrete vortex rings) are then expected to be weak (as also known from experiments). Accordingly, quadrupole sources will be ignored in the following, and only monopoles and dipoles will be considered.

Returning to cylindrical polar coordinates, the sound field generated by the hole-tone system is then modelled by application of the following simplified version of (20) (valid when the observation point (x,r) is within the fluid):

$$\frac{1}{c_0^2}\frac{\partial^2 p}{\partial t^2}-\nabla^2 p=-\nabla\cdot\mathbf{f}+\rho_0\frac{\partial\hat{u}}{\partial t}, \tag{23}$$

where $\nabla\cdot$ is the divergence operator and

$$\mathbf{f}(t,x,r)=(f_x,\, f_r)=(f_x(r),0)\delta(x-x_s) \tag{24}$$

is a fluid force (per unit volume) acting at $x = x_s$, $r_0 < r < r_{\text{plate}}$. $\delta(x - x_s)$ is the usual, 1D (Dirac) delta function. Similarly, the flow speed $\hat{u}$ at $x = x_s$, $0 < r < r_0$, is written as

$$\hat{u} = u_r(r)\delta(x - x_s). \tag{25}$$

3.2. Solution by Fourier transform

As Eq. (23) is linear, monopole and dipole pressure contributions can be solved for apart, and added to give the total acoustic pressure. For clarity, only the solution for the dipole contribution will be shown in detail.

Fourier transforms with respect to time and space are defined as

$$\begin{aligned} p(t, x, r) &= \int_{-\infty}^{\infty} P(\omega, x, r)\mathrm{e}^{-\mathrm{i}\omega t}\,\mathrm{d}\omega, \\ P(\omega, x, r) &= \frac{1}{2\pi}\int_{-\infty}^{\infty} p(t, x, r)\mathrm{e}^{\mathrm{i}\omega t}\,\mathrm{d}t, \end{aligned} \tag{26}$$

and

$$\begin{aligned} P(\omega, x, r) &= \frac{1}{2\pi}\int_{-\infty}^{\infty} \mathscr{P}(\omega, \zeta, r)\mathrm{e}^{-\mathrm{i}\zeta x}\,\mathrm{d}\zeta, \\ \mathscr{P}(\omega, \zeta, r) &= \int_{-\infty}^{\infty} P(\omega, x, r)\mathrm{e}^{\mathrm{i}\zeta x}\,\mathrm{d}x, \end{aligned} \tag{27}$$

respectively. Here $\mathrm{i} = \sqrt{-1}$, ω is an angular velocity, and ζ is the axial wavenumber. Using Eq. (26) the governing (23) is converted into the reduced wave equation (considering the dipole term only)

$$\nabla^2 P + k^2 P = \nabla \cdot \tilde{\mathbf{f}}, \tag{28}$$

where $k = \omega/c_0$ is the acoustic wavenumber, and $\tilde{\mathbf{f}}$ is the Fourier transform of $\mathbf{f}$. By using Eq. (27) and integration by parts on the right-hand side, Eq. (28) can be converted into the ordinary differential equation

$$\frac{\partial^2 \mathscr{P}}{\partial r^2} + \frac{1}{r}\frac{\partial \mathscr{P}}{\partial r} + (k^2 - \zeta^2)\mathscr{P} = -\mathrm{i}\zeta\tilde{f}_x(r)\mathrm{e}^{\mathrm{i}\zeta x_s}. \tag{29}$$

Note that $\tilde{f}_x$ is now a surface stress (pressure) due to the integration over x.

The free-space (out-going wave) solution to

$$\frac{\partial^2 G}{\partial r^2} + \frac{1}{r}\frac{\partial G}{\partial r} + \kappa^2 G = \frac{\delta(r - r^*)}{\pi r} \tag{30}$$

is given by the Green's function [33]

$$G(r, r_*) = -\frac{\mathrm{i}}{4} H_0^{(1)}(\kappa|r - r^*|), \tag{31}$$

where $H_0^{(1)}$ is the Hankel function of first kind and zeroth order. [In Eq. (30), $\delta(r - r^*)/\pi r$ is the axisymmetric delta function, defined such that $\int_0^\infty \mathscr{F}(r)\delta(r - r^*)\,\mathrm{d}r = \frac{1}{2}\mathscr{F}(r^*)$, where $\mathscr{F}$ is any good function of r [34].] The solution of (29) is then given by

$$\mathscr{P}(\omega,\zeta,r) = -\int_0^\infty \mathrm{i}\zeta\tilde{f}_x(\hat{r})\mathrm{e}^{\mathrm{i}\zeta x_s}G(r,\hat{r})2\pi\hat{r}\,\mathrm{d}\hat{r} \approx -\sum_n \frac{1}{4}\zeta\tilde{f}_{xn}\mathrm{e}^{\mathrm{i}\zeta x_s}H_0^{(1)}(\sigma|r-r_n|), \quad \sigma^2 = k^2-\zeta^2. \tag{32}$$

Here $\tilde{f}_{xn}$ is the Fourier transform of discrete fluid forces[4] f_{xn}, defined as follows. The section between two consecutive bound vortex rings (on the end plate) is considered as a hollow circular plate-shaped panel. The pressure p_{hn} acting on the nth panel is evaluated at a central control point by using the unsteady Bernoulli equation [19],

$$p_{hn} = -\rho_0\left(\frac{1}{2}u_{rn}^2 + \frac{\partial\Phi_n}{\partial t}\right), \tag{33}$$

excluding reference pressure and velocity at infinity, which are assumed to be zero. The velocity potential Φ_n is evaluated by integrating up the radial velocity using the midpoint rule,

$$\Phi_n = \int_{r_0}^{r_n} u_r\,\mathrm{d}r \approx \sum_{j=1}^{n} b_j u_r(j), \tag{34}$$

where b_j is the breadth of the jth panel and $u_r(j)$ indicates evaluation at the jth control point. The time derivative is evaluated by a finite difference approach,

$$\frac{\partial\Phi_n}{\partial t} \approx \frac{(\Phi_n)_t - (\Phi_n)_{t-\Delta t}}{\Delta t}. \tag{35}$$

The pressure is assumed to be constant over each panel. The equivalent ring force f_{xn} acting at the mean panel radius is then evaluated as

$$f_{xn} = 2\pi r_n b_n p_{hn}, \tag{36}$$

where r_n is the mean radius of the nth panel. The integral in Eq. (32) is thus also evaluated by the midpoint rule. It is noted here that only the pressure on the side of the end plate facing the nozzle is taken into consideration, not the pressure difference across the plate. The pressure fluctuations on the backside of the plate are assumed to be small.

From Eq. (32) the solution of Eq. (28) is obtained by Fourier inverse transform as

$$P(\omega,x,r) = -\sum_n \frac{1}{8\pi}\tilde{f}_{xn}\int_{-\infty}^{\infty} \mathrm{e}^{\mathrm{i}\zeta(x_s-x)}H_0^{(1)}(\sigma|r-r_n|)\zeta\,\mathrm{d}\zeta. \tag{37}$$

Considering the integration contour running from $-\infty$ to ∞ along the real axis in the complex ζ-plane, the function $\sigma = (k^2-\zeta^2)^{1/2}$ has branch points at $\zeta = -k, k$. Branch cuts above $-k$ and below $+k$ ensure a decaying pressure amplitude for $\zeta < -k$ and $\zeta > k$ as $r \to \infty$, because then the

---

[4] Forces from now on (rather than pressure) due to the integration of over the plane $x = x_s$.

function σ takes the values

$$\sigma = \begin{cases} \mathrm{i}\sqrt{\zeta^2 - k^2} & \text{for } \zeta < -k, \\ \sqrt{k^2 - \zeta^2} & \text{for } -k < \zeta < k, \\ \mathrm{i}\sqrt{\zeta^2 - k^2} & \text{for } \zeta > k. \end{cases} \tag{38}$$

The integral in Eq. (37) can be evaluated analytically, see Appendix B. By introducing the variables

$$R_n = |r - r_n|, \quad X = |x_s - x|, \quad D_n^2 = R_n^2 + X^2, \tag{39}$$

the result can be written as

$$P(\omega, x, r) = -\sum_n \frac{\tilde{f}_{xn}}{4\pi} \frac{X}{D_n^2} \left(\frac{1}{D_n} - \mathrm{i}k \right) \mathrm{e}^{\mathrm{i}D_n k}. \tag{40}$$

Finally, application of the Fourier inverse transform on Eq. (40) gives the physical dipole pressure $p_{\mathrm{di}}(t, x, r)$ as

$$p_{\mathrm{di}}(t, x, r) = -\sum_n \frac{X}{4\pi c_0 D_n^2} \left[\frac{c_0}{D_n} f_{xn} + \frac{\partial f_{xn}}{\partial t} \right]_{\tau_n}, \tag{41}$$

where the terms in the square bracket with subscript τ_n are to be evaluated at the retarded time $\tau_n = t - D_n/c_0$.

Similarly, the pressure from the monopole term in Eq. (23) is evaluated as

$$p_{\mathrm{mono}}(t, x, r) = \rho_0 \int_0^{r_0} \frac{1}{4\pi D(r)} \left[\frac{\partial u_r}{\partial t} \right]_{\tau_n} 2\pi r \,\mathrm{d}r \approx \rho_0 \sum_n \frac{\mathscr{A}_n}{4\pi D_n} \left[\frac{\partial u_r(r_n)}{\partial t} \right]_{\tau_n}, \tag{42}$$

where, as in Eq. (34), the integral is approximated numerically using the midpoint rule. Here r_n is the radius from the center to the nth control point, and $\mathscr{A}_n$ is the ring area having r_n as mean radius. D_n has the same meaning here as specified by Eq. (39).

It is interesting to note that Eq. (41) has exactly the same form in rectangular coordinates, see e.g. [35], Eq. (2). The axisymmetric 'nature' is hidden in the definitions given by Eqs. (36) and (39). [The same applies to Eq. (42).]

It must be noted that, although no far-field approximations have been introduced, evaluation of the acoustic pressure well within the outer edge of the end plate is likely to be unreliable. As explained by Powell [5], if the extent of the plate was beyond the sound generating flow (and the hole is ignored for the moment) the contribution from an image system should be added to the acoustic pressure (making up a 'double source system', symmetric about the end plate). Considering Eq. (41) it can be seen that the latter contribution will be equal to the contribution from the physical sources, but with opposite sign, resulting in a complete cancellation of the dipole pressure. In the present problem there is a hole in the plate, and the sound generating flow extends to envelop the outer edge, so dipole sources will remain at both the inner and the outer edge. But in between only quadrupole sources will survive. So use of Eq. (41) in this domain will overestimate the acoustic pressure level.

A quantitatively improved calculation of the sound pressure in the near-field domain can perhaps be obtained by basing the solution to the acoustic problem on the exact Green's function, G^* say, which satisfies the boundary condition $\partial G^*/\partial \mathrm{n} = 0$ on the end plate. The assumption that the plate is acoustically compact will simplify G^*. Application of Howe's vortex sound equation [7,32] instead of (20) may also be of advantage.

4. An acoustic feedback mechanism

The acoustic velocity potential function $\psi(t, x, r)$ can be obtained from the pressure function $p(t, x, r)$ as [36]

$$\frac{\partial \psi}{\partial t} = \frac{p}{\rho_0} \quad \Leftrightarrow \quad \psi = \frac{1}{\rho_0} \int p \, \mathrm{d}t + q(x, r). \tag{43}$$

We choose the integration 'constant' $q(x, r) \equiv 0$ such that $\psi = 0$ for $t \leqslant 0$. The acoustic perturbation velocity is obtained as

$$\mathbf{v} = (v_x, v_r) = -\nabla \psi = \left(-\frac{\partial \psi}{\partial x}, -\frac{\partial \psi}{\partial r} \right). \tag{44}$$

As in the last section details are shown for the dipole contribution. Only the final result is given for the monopole contribution. Let $\tilde{\psi}_n$ denote the velocity potential in the frequency domain, corresponding to the nth force composant. This is obtained from Eq. (40) as

$$\tilde{\psi}_n(\omega, x, r) = -\frac{\tilde{f}_{xn}}{4\pi} \frac{X}{\rho c_0 D_n^2} \left(1 + \mathrm{i} \frac{c_0}{\omega D_n} \right) \mathrm{e}^{\mathrm{i} D_n \omega / c_0}. \tag{45}$$

Use of the Fourier inverse transform gives the time-domain solution as

$$\psi_n(t, x, r) = -\frac{X}{4\pi \rho c_0 D_n^2} \left([f_{xn}]_{\tau_n} + \frac{c_0}{D_n} \mathscr{I}_f \right), \tag{46}$$

where

$$\mathscr{I}_f(t) = \int_{-\infty}^{t} f_{xn}(\hat{t} - D_n/c_0) \, \mathrm{d}\hat{t}. \tag{47}$$

[This follows directly by consideration of Eq. (41) but, for completeness, a formal derivation of this term is shown in Appendix C.] Eq. (44) then gives the final expressions

$$\begin{aligned} v_{x,\mathrm{di}} &= \sum_n \frac{1}{4\pi \rho_0 c_0 D_n^2} \left\{ \left(1 - 3 \frac{X^2}{D_n^2} \right) \left([f_{xn}]_{\tau_n} + \frac{c_0}{D_n} \mathscr{I}_f \right) - \frac{X^2}{D_n c_0} \left[\frac{\partial f_{xn}}{\partial t} \right]_{\tau_n} \right\}, \\ v_{r,\mathrm{di}} &= -\sum_n \frac{X R_n}{4\pi \rho_0 c_0 D_n^3} \left\{ \frac{3}{D_n} [f_{xn}]_{\tau_n} + \frac{3 c_0}{D_n^2} \mathscr{I}_f + \frac{1}{c_0} \left[\frac{\partial f_{xn}}{\partial t} \right]_{\tau_n} \right\}. \end{aligned} \tag{48}$$

In the calculations, the term $\mathscr{I}_f$ is evaluated by solving numerically the differential equation

$$\frac{\partial \mathscr{I}_f}{\partial t} = f_{xn} \tag{49}$$

with the initial condition $\mathscr{I}_f = 0$ at $t = 0$. This is done by using Acton's second-order approach [20]

$$\mathscr{I}_f(t + \Delta t) := \mathscr{I}_f(t) + (3f_{xn}(t) - f_{xn}(t - \Delta t))\tfrac{1}{2}\Delta t. \tag{50}$$

The term $\partial f_{xn}/\partial t$ is evaluated using the finite difference approach (35). It is noted that the zero-frequency component of f_{xn}, $n = 1, 2, \ldots$, will generate a steady, non-physical 'feedback flow'. To avoid this a time-domain filter is applied to f_{xn}. Further details are described in Section 6.

The monopole pressure (42) gives the velocity contributions

$$\begin{aligned} v_{x,\text{mono}} &= -\sum_n \frac{X\mathscr{A}_n}{4\pi D_n^2}\left\{\frac{1}{D_n}[u_r]_{\tau_n} + \frac{1}{c_0}\left[\frac{\partial u_r}{\partial t}\right]_{\tau_n}\right\}, \\ v_{r,\text{mono}} &= \sum_n \frac{R_n\mathscr{A}_n}{4\pi D_n^2}\left\{\frac{1}{D_n}[u_r]_{\tau_n} + \frac{1}{c_0}\left[\frac{\partial u_r}{\partial t}\right]_{\tau_n}\right\}, \end{aligned} \tag{51}$$

where the symbols are as defined by Eq. (42).

The acoustic velocities acts as disturbances to the hydrodynamic velocity field near the nozzle exit, at $x = x_e$. In the numerical scheme the disturbances are applied to the free vortex rings present within a specified influence distance x_{id} from x_e, as corrections to the positions and radii (x_i, r_i), according to the following law:

$$\text{If} \quad x_e < x_i \leqslant x_e + x_{id} \quad \text{then} \quad x_i := x_i + v_x \Delta t, \quad r_i := r_i + v_r \Delta t. \tag{52}$$

5. Forced acoustic excitation

Forced acoustic excitation by a loudspeaker is simulated by adding the disturbance velocity

$$v_r = A_d u_0 \cos(2\pi f_d t), \tag{53}$$

where A_d is a non-dimensional amplitude factor and f_d is the excitation frequency. This disturbance is also applied according to Eq. (52) (with $v_x = 0$).

6. Computational aspects

6.1. Geometry of an experimental setup

Numerical results will be discussed for geometric and physical data corresponding to an experimental setup with nozzle and end plate hole diameter d_0 equal to 50 mm. In the numeric model the outer diameter of the end plate is taken to be 250 mm (although the experimental end plate is different; see Section 8.1). The reference gap length L is 50 mm. Variation of L between d_0 (50 mm) and $2.5d_0$ (125 mm) will be studied in Section 8.2. The reference mean velocity u_0 of the air-jet is 10 m/s. At 20 °C this corresponds to a Reynolds number $Re = u_0 d_0/\nu \approx 3.3 \times 10^4$ and a Mach number $M = u_0/c_0 \approx 0.03$, where the speed of sound $c_0 = 340\,\mathrm{m/s}$ and the kinematic viscosity $\nu = 1.5 \times 10^{-5}\,\mathrm{m^2/s}$. Variation of u_0 between 10 and 25 m/s will also be studied in Section 8.2.

Discussions of numerical results will be referred to a coordinate system (x, r) with origo at the nozzle exit (before denoted by x_e). In this coordinate system the nozzle exit is thus located at $x = 0$ and the end plate at $x = L$.

6.2. The hydrodynamic part of the analysis

In the computations to be presented, the length of the exit pipe is $2.5d_0$. [The outer radius of the end plate is also $2.5d_0$, as mentioned before.] The number of vortex rings on the flow-providing upstream end of the exit pipe $N_{ev} = 6$. The number of vortex rings covering the exit pipe surface and the end plate is $N_{\mathrm{pipe}} = 24$ and $N_{\mathrm{plate}} = 24$, respectively. It has been verified this discretization is sufficiently fine, and that the hole-tone dynamics is insensitive to changes in these parameters. With the given values of N_{ev}, N_{pipe}, and N_{plate}, the equation system (8) is of size 54×54. It is solved at each time step using the LU decomposition method [29].

The vortex updating scheme requires $O(N_\Sigma^2)$ evaluations at each time step, with N_Σ vortex rings involved. In order to reduce the computation time, the influence on any free vortex from other free vortices further away than ten nozzle diameters is ignored. It has been verified that this has negligible influence on the resulting convection velocities, or any other aspect of the vortex dynamics. Complete removal of vortex rings is not done; this was found to cause numerical instability.

Vortex shedding from the edge of the end plate was included in the initial numerical computations, but was found to have no influence on the vortex dynamics between nozzle and end plate. It is therefore not included in the results to be presented. Vortex shedding from the outer edge of the end plate is also ignored.

The basic time step is chosen to be $\Delta t = 0.025 d_0/u_0$. This corresponds, if vortex roll-up is ignored for the moment, to discretization of the shear layer between nozzle and end plate into 40 equidistant vortex rings. Results obtained with $\Delta t = 0.05 d_0/u_0$ and $0.0125 d_0/u_0$ will also be shown, to confirm that the value $0.025 d_0/u_0$ is sufficiently small. Adaptive step-size control in the Runge–Kutta method may increase both accuracy and computation speed. But the interest here is in the frequency spectrum, and analysis with a standard fast Fourier transform method requires evenly spaced time intervals. [This problem could of course be managed by recording data only at times conforming with one particular value of Δt, but this has not been done here.] Simulations were performed with between 1500 and 2400 time steps, in order to obtain transient-free frequency spectra of fluctuating velocities and acoustic pressures. Of the 1500 to 2400 time steps, the last $2^{10} = 1024$ steps were analyzed by fast Fourier transform; the first 476 to 1376 steps were discarded, as transients.

With $\Delta t = 0.025 d_0/u_0$ the Nyquist criterion gives the maximum 'useful' frequency $f_{\max} = 1/(2\Delta t) = 20 u_0/d_0$. With $u_0 = 10\,\mathrm{m/s}$ and $d_0 = 0.05\,\mathrm{m}$ this gives $f_{\max} = 4\,\mathrm{kHz}$.

The relative smallness of the equation system hints that single precision calculations may be sufficient [29,19]. To check this, calculations were performed in both single and double precision. These were carried out using a VT WSi computer with Pacific-Sierra Research's VAST Fortran 90 compiler, running on an Intel Pentium IV 2.8 GHz processor. A few calculations were also done in quadruple precision, using Fujitsu's Fortran 90 compiler running on an UltraSparc 300 MHz processor. A simulation running 2400 time steps required approximately 24 h on the VT WSi computer.

6.3. The acoustic part of the analysis

As mentioned in Section 4, if the mean value of each f_{xn} $(n = 1, 2, \ldots)$, is not exactly zero (i.e., if the zero frequency Fourier composant of f_{xn} is not zero) a non-physical feedback flow will be generated. To avoid this, a (time-domain) linear, recursive bandpass filter [29, p. 552] is applied to f_{xn}. Lower and upper cutoff frequencies are set to 10 Hz and 10 kHz, respectively. Eliminating the spurious very-low-frequency content from the acoustic fluid force is plausible from a physical point-of-view, since Eq. (40) shows that, in reality, there is no noise contribution (and thus no contribution to the acoustic feedback) for $\omega = 0$. The very-high-frequency content ($>f_{\max}$) also is not of use.

The discretization of integral (32) can be viewed as a simple boundary element discretization into 'lumped' elements, with a central control point, and constant mechanical properties within each element. The length of each element is (0.1/24) m ≈ 0.004167 m. It is recommended for boundary element analysis [37] that the nodal distances should be smaller than the speed of sound c_0 times the time step Δt. With $\Delta t = 0.025 d_0/u_0$, $u_0 = 10\,\mathrm{m/s}$, and $d_0 = 0.05\,\mathrm{m}$, $\Delta t \times c_0 = 0.000125\,\mathrm{s} \times 340\,\mathrm{m/s} = 0.0425\,\mathrm{m}$, which indeed is much larger than the element length of 0.004167 m. For solution of acoustic (and other wave-related) problems with the finite element method it is recommended that the element lengths should be smaller than $\frac{1}{10}$th of the minimum wavelength [38]. Applying this criterion to the present analysis it is noted that the interest is in frequencies smaller than 1 kHz. The smallest acoustic wavelength is thus $\lambda_{\min} = 0.34\,\mathrm{m}$, and $\lambda_{\min}/10 = 0.034\,\mathrm{m}$ which also is much larger than the element length. Finally, it is noted that the integral in Eq. (42) is evaluated using ten subintervals.

In the calculations to follow the retarded time corrections D_n/c_0 are always very small, and will be neglected. [See Eq. (41) and the explanation following this equation.]

7. Numerical results

7.1. Computations without acoustic feedback

7.1.1. Influence of smoothing parameter ε

Fig. 3 shows the computed distribution of vortex rings during one period, based on the characteristic (dominating) frequency f (explained a little later). The shown domain is $0 \leqslant x \leqslant 2d_0$, $-d_0 \leqslant y \leqslant d_0$. The nozzle exit is thus just on the left frame-line and the end plate is in the center of the figure parts. The results were obtained with smoothing parameter $\varepsilon = 0.05 d_0$. The sequence indicates how the shear layer surrounding the jet rolls up into distinct, big vortices ('smoke rings') which separate from the shear layer and hit the end wall, for then to spread outward, and move over the plate. The simulated sequence agrees well with the sketch and description given in Ref. [2] (Fig. 1, p. 903, and 'Section A. Preliminary Observations', p. 905). The frequency of vortex

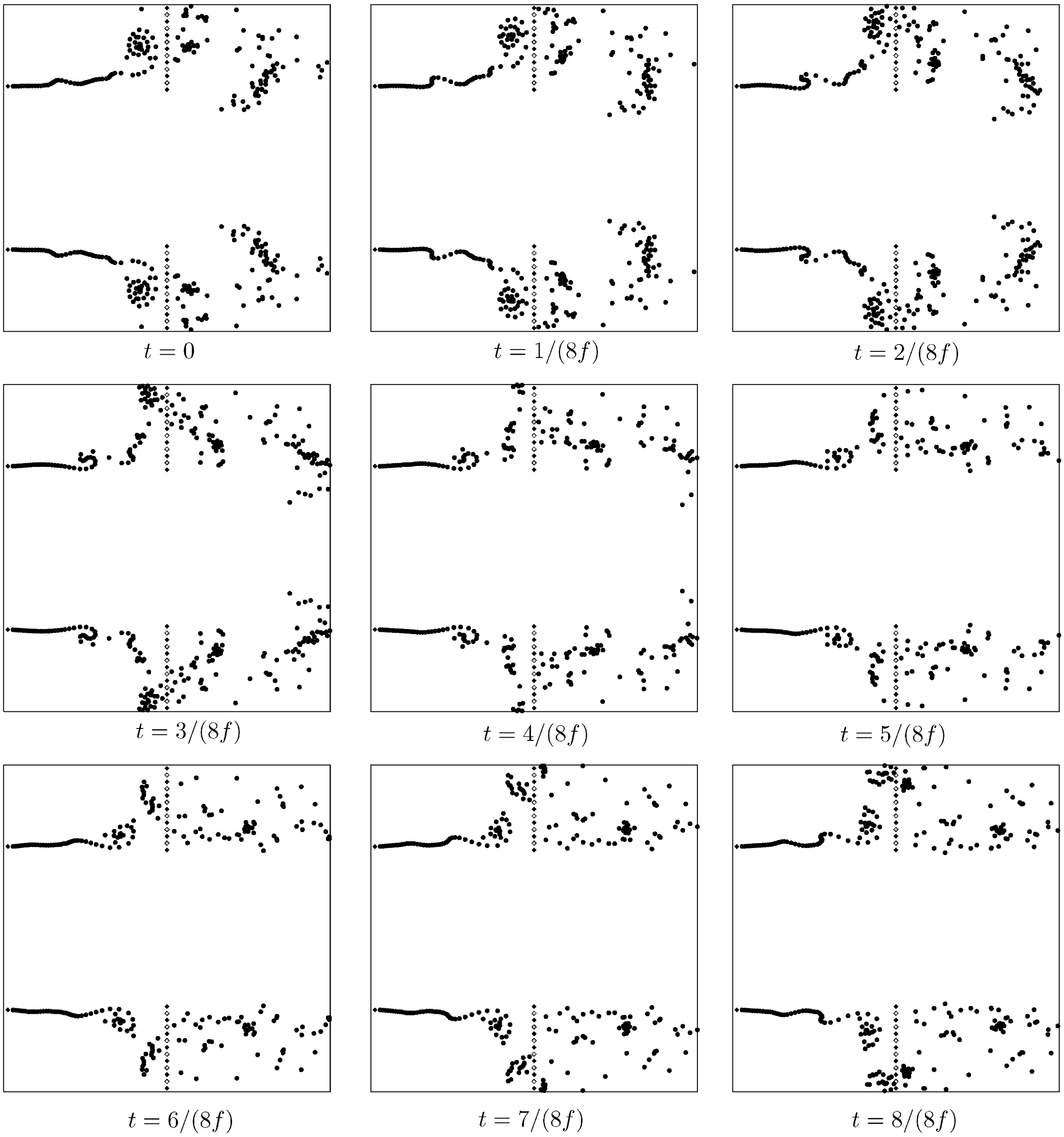

Fig. 3. Simulation of the jet with $\varepsilon = 0.05d_0$. Vortex shedding from the end plate is not included. The nozzle exit is located on the left frame of the figure parts. The end plate is seen in the center. One period of oscillation is shown.

formation equals 203.3 Hz, corresponding to a Strouhal number $St = fL/u_0 \approx 1.0$. It will be seen a little later that this frequency also is dominating in the acoustic spectrum, and is thus identified with the characteristic *hole-tone frequency*.

Figs. 4 and 5 show similar sequences for $\varepsilon = 0.1d_0$ and $0.125d_0$, respectively. Increasing ε implies limitation of the roll-up, from a tightly rolled-up smoke ring for $\varepsilon = 0.05d_0$ to just a single

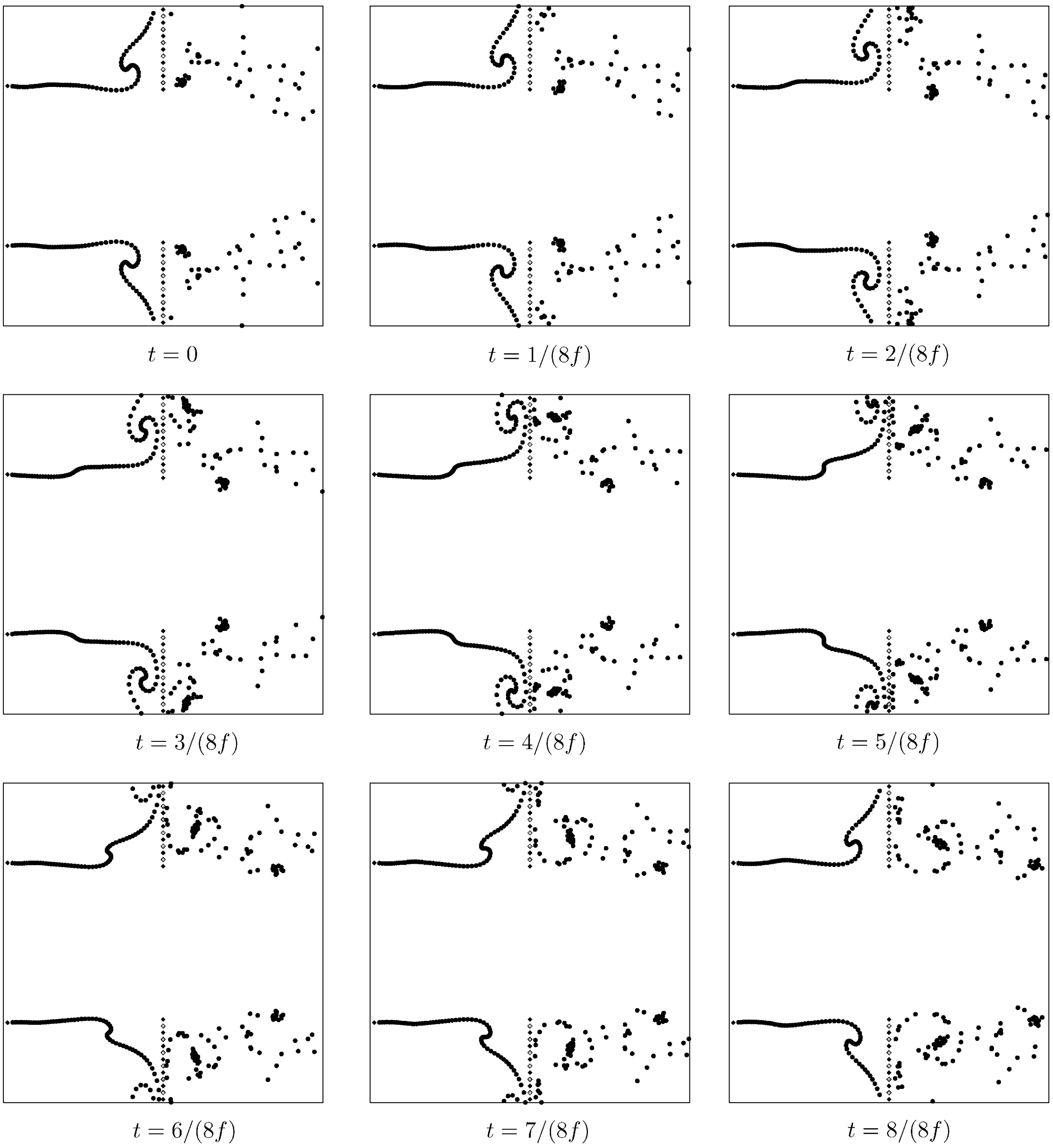

$t = 0$ $t = 1/(8f)$ $t = 2/(8f)$

$t = 3/(8f)$ $t = 4/(8f)$ $t = 5/(8f)$

$t = 6/(8f)$ $t = 7/(8f)$ $t = 8/(8f)$

Fig. 4. As Fig. 3 but with $\varepsilon = 0.1d_0$.

curl for $\varepsilon = 0.125d_0$. The hole-tone frequency is however not affected much; it is also 203.3 Hz for $\varepsilon = 0.1d_0$, and 187.6 Hz for $\varepsilon = 0.125d_0$.

Figs. 6 and 7 show the vorticity field (6) for $\varepsilon = 0.05d_0$ and $0.125d_0$, respectively, corresponding to Figs. 3 and 5. [Note that the end plate is not shown. Its location can be seen from Figs. 3 and 5, as the plotting domain is the same.] It is seen that increasing ε results in thickening of the vorticity

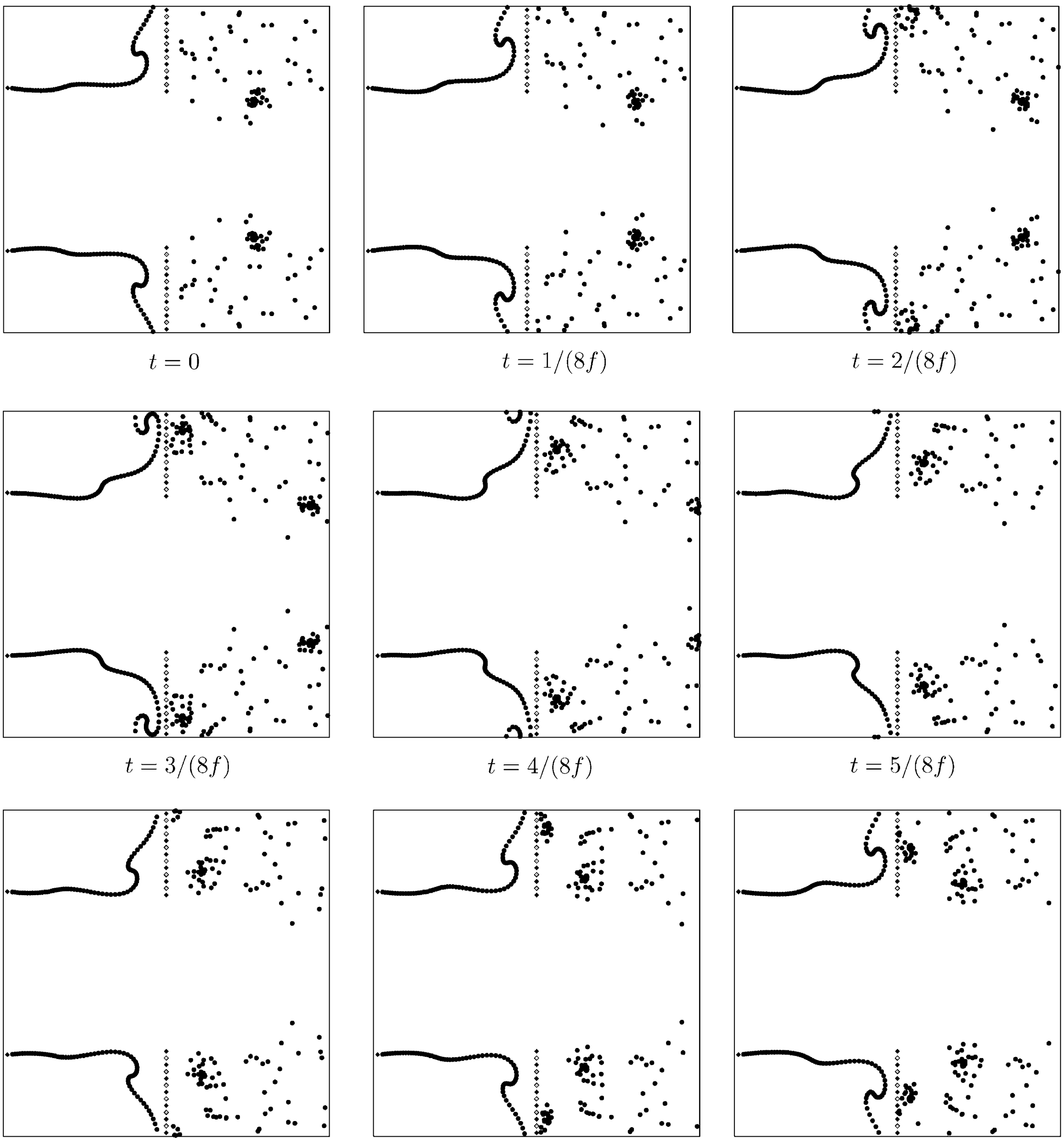

$t = 0$ $t = 1/(8f)$ $t = 2/(8f)$

$t = 3/(8f)$ $t = 4/(8f)$ $t = 5/(8f)$

$t = 6/(8f)$ $t = 7/(8f)$ $t = 8/(8f)$

Fig. 5. As Fig. 3 but with $\varepsilon = 0.125d_0$.

layer. In this sense the smoothing parameter ε acts as viscosity, as discussed in Section 2.1. Figs. 6 and 7 verify the indication given by Figs. 3–5 that the shear layer rolls up into big, distinct vortex rings. [Aref [39, p. 380] warns that apparent vortex roll-up, as indicated by discrete vortex markers, may sometimes be misleading.].

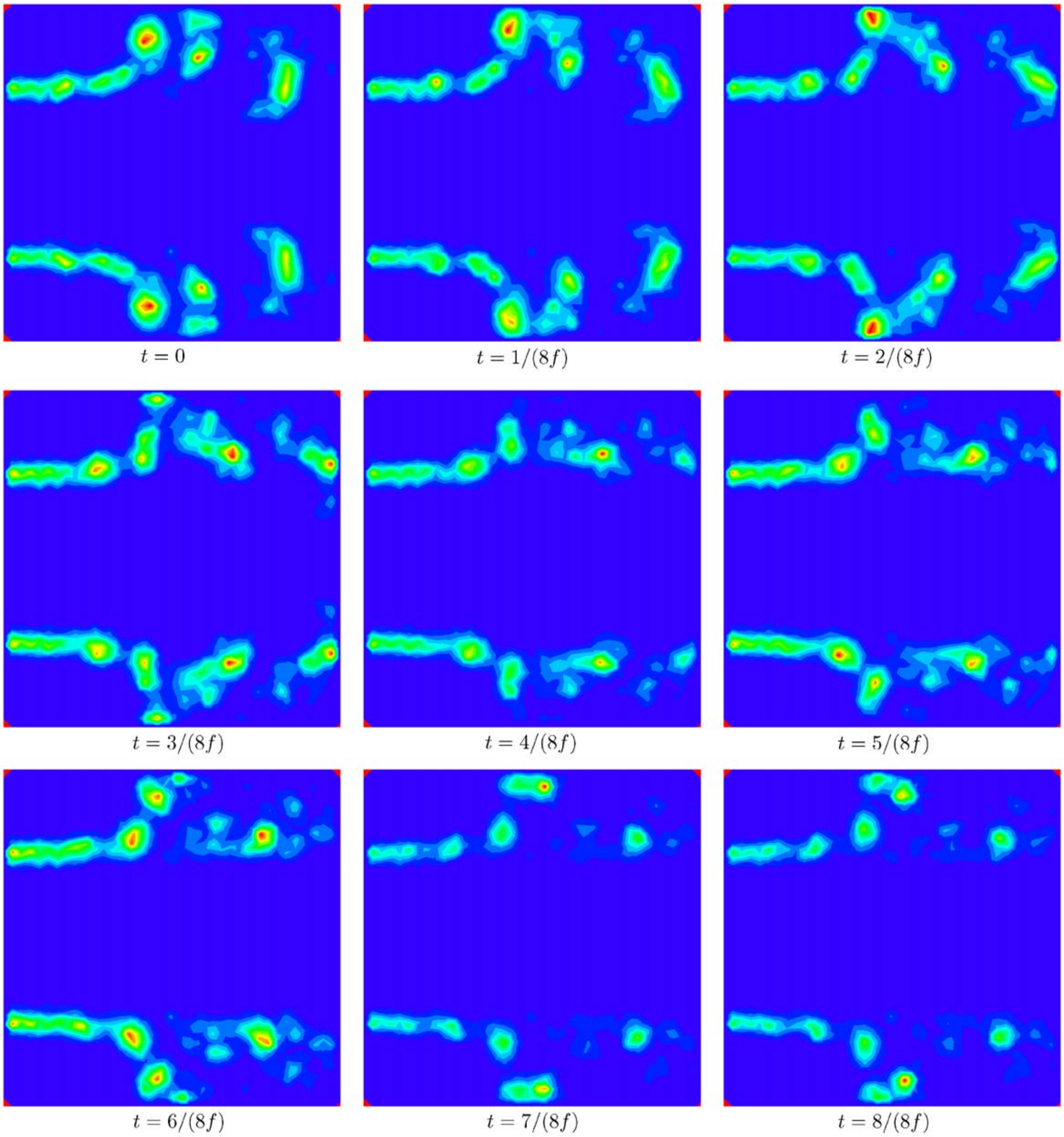

$t = 0$ $t = 1/(8f)$ $t = 2/(8f)$

$t = 3/(8f)$ $t = 4/(8f)$ $t = 5/(8f)$

$t = 6/(8f)$ $t = 7/(8f)$ $t = 8/(8f)$

Fig. 6. Iso-vorticity levels for the jet with $\varepsilon = 0.05d_0$. The shown sequence fits the simulation in Fig. 3; the plotting domain is also the same. [Note that the end plate is not shown. Its location can be seen from Fig. 3.]

Fig. 8 shows the acoustic dipole and monopole pressure signals at the positions $(x, r) = (0.5, 5)d_0$ (part a) and $(x, r) = (0.0, 0.5)d_0$ (part b), for $\varepsilon = 0.125d_0$. It is seen that the monopole contribution is much smaller than the dipole contribution. The difference is most pronounced near the nozzle (part b). The monopole contribution is thus ignored in the results to follow.

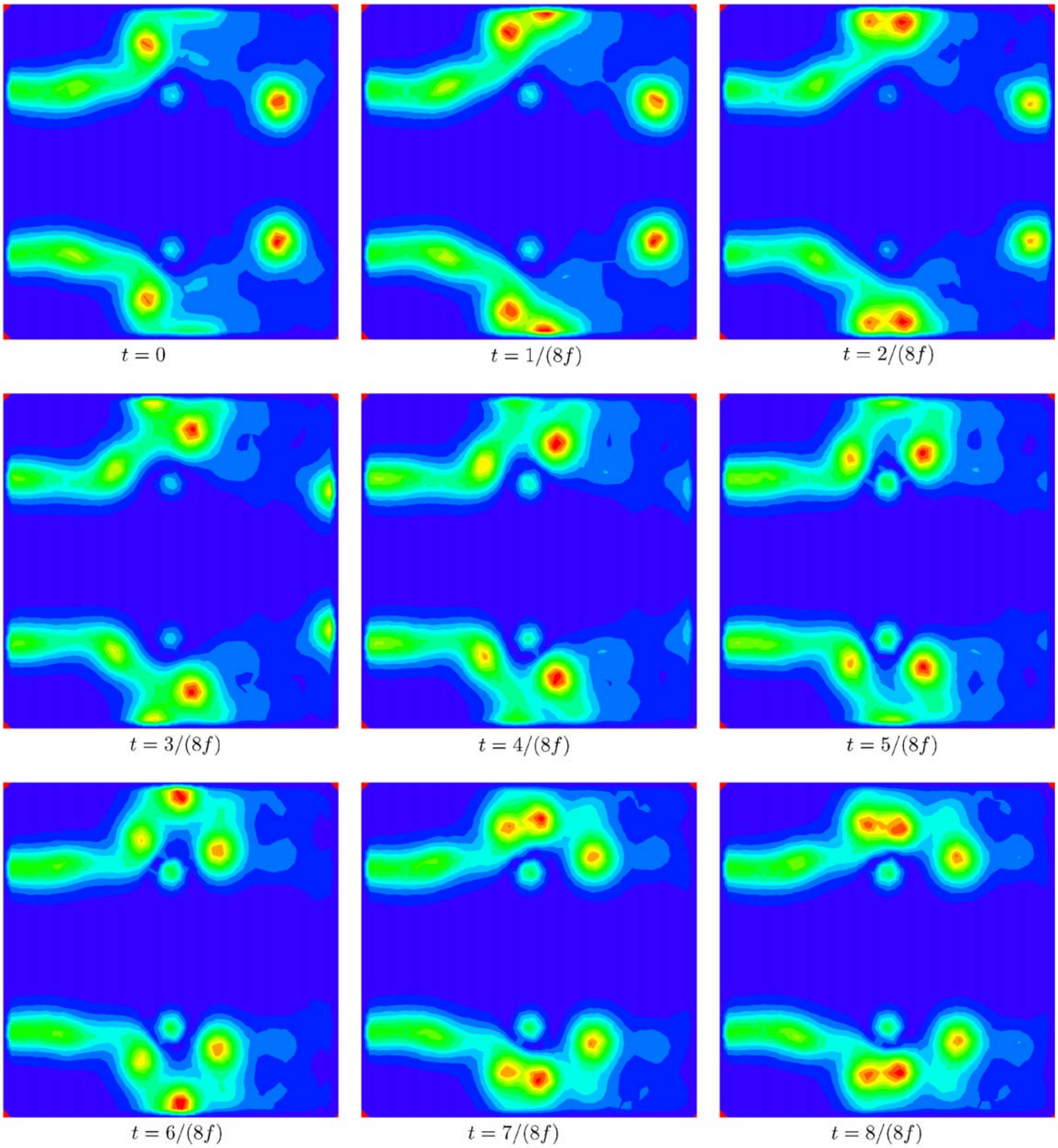
$t = 0$ $t = 1/(8f)$ $t = 2/(8f)$

$t = 3/(8f)$ $t = 4/(8f)$ $t = 5/(8f)$

$t = 6/(8f)$ $t = 7/(8f)$ $t = 8/(8f)$

Fig. 7. Iso-vorticity levels for the jet with $\varepsilon = 0.125d_0$. The shown sequence fits the simulation in Fig. 5; the plotting domain is also the same. [Note that the end plate is not shown. Its location can be seen from Fig. 5.]

Fig. 9 shows the acoustic (dipole) pressure level (41), (in dB; reference pressure $p_{\text{ref}} = 2 \times 10^{-5}\,\text{N/m}^2$) at the position $(x, r) = (0.5, 5)d_0$, for values of ε ranging from $0.025d_0$ to $0.13d_0$. The values of the characteristic (dominating) frequency f for the different values of ε are listed in Table 1. It is noticed from Fig. 9 that second and third harmonic of f come out quite clear for $\varepsilon = 0.11d_0 \ldots 0.125d_0$.

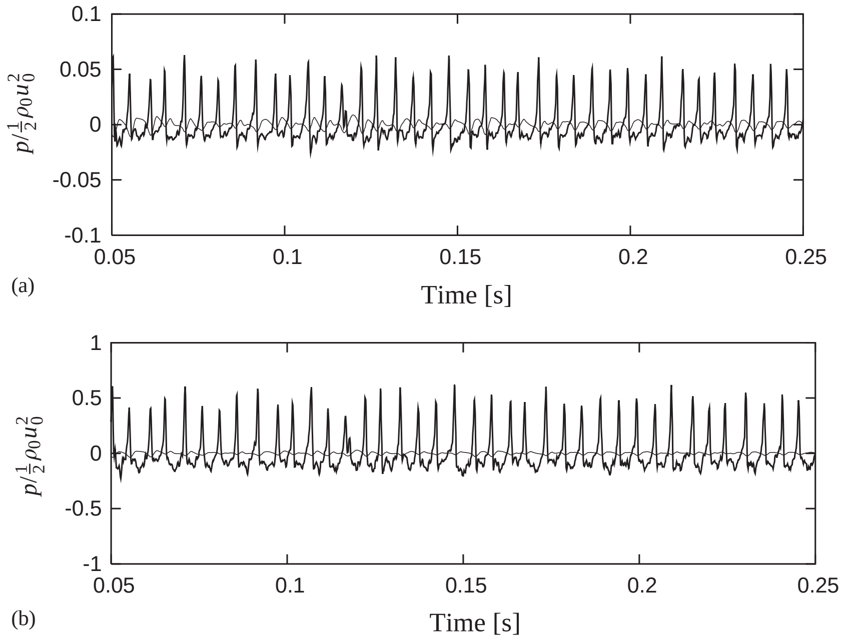

Fig. 8. (a) Sound pressure at the position $(x, r) = (0.5, 5)d_0$; (b) The same at the position $(x, r) = (0.0, 0.5)d_0$. Thick line (and largest amplitude): dipole pressure p_{di}; thin line (and smallest amplitude): monopole pressure p_{mono}.

Increasing the value of ε reduces the broad-band noise level. This is because the 'artificial viscosity' associated with this parameter damps out the small-scale random ('chaotic') motions of the individual vortex rings [39]. Comparison of Figs. 3–5 also gives a good indication of this.

As mentioned in Section 1, the shear layer convection velocity u_c is typically $0.6u_0 - 0.7u_0$. Computed vortex ring convection velocities are shown in Fig. 10. It is noted that the axial velocities are shown. As seen from Figs. 3–5, near the end plate the vortices bend off and move over it. This is why the depicted axial velocities go towards zero there. The computed values are too high for $\varepsilon = 0.025d_0 \ldots 0.11d_0$, but reasonable for $\varepsilon \geqslant 0.115d_0$. It is interesting to note that the changes in vortex convection velocities does not seriously affect the hole-tone frequency (see Fig. 9). Considering the mean value of u_c in the range $0 \leqslant x \leqslant 0.8L$, of the four 'good' cases the following values are estimated: $u_c \approx 0.7u_0$ for $\varepsilon = 0.115d_0$ and $0.12d_0$, and $u_c \approx 0.65u_0$ for $\varepsilon = 0.125d_0$ and $0.13d_0$.

Fig. 11 shows the hole-tone frequency f as function of the non-dimensional convection velocity u_c/u_0, calculated according to Eq. (1) for $n = 1$ (lower curve), $\frac{3}{2}$ (middle curve), and 2 (upper curve). Inserting the just mentioned vortex convection velocities and the hole-tone frequencies found from Fig. 9, it is seen that the three cases $\varepsilon = 0.115d_0, 0.12d_0$, and $0.125d_0$ fit the $n = \frac{3}{2}$ curve quite well ($\varepsilon = 0.125d_0$ in particular). Returning at this point to the discussion of (1) and to Figs. 3–5, it can be verified that the distance between the individual smoke rings (big vortices) $\sim \frac{2}{3}L$.

Figs. 12–15 illustrate how the smoothing parameter ε affects the hydrodynamic pressure level (HPL) and velocity fluctuation level (VFL) at various locations. Figs. 12 and 13 show the

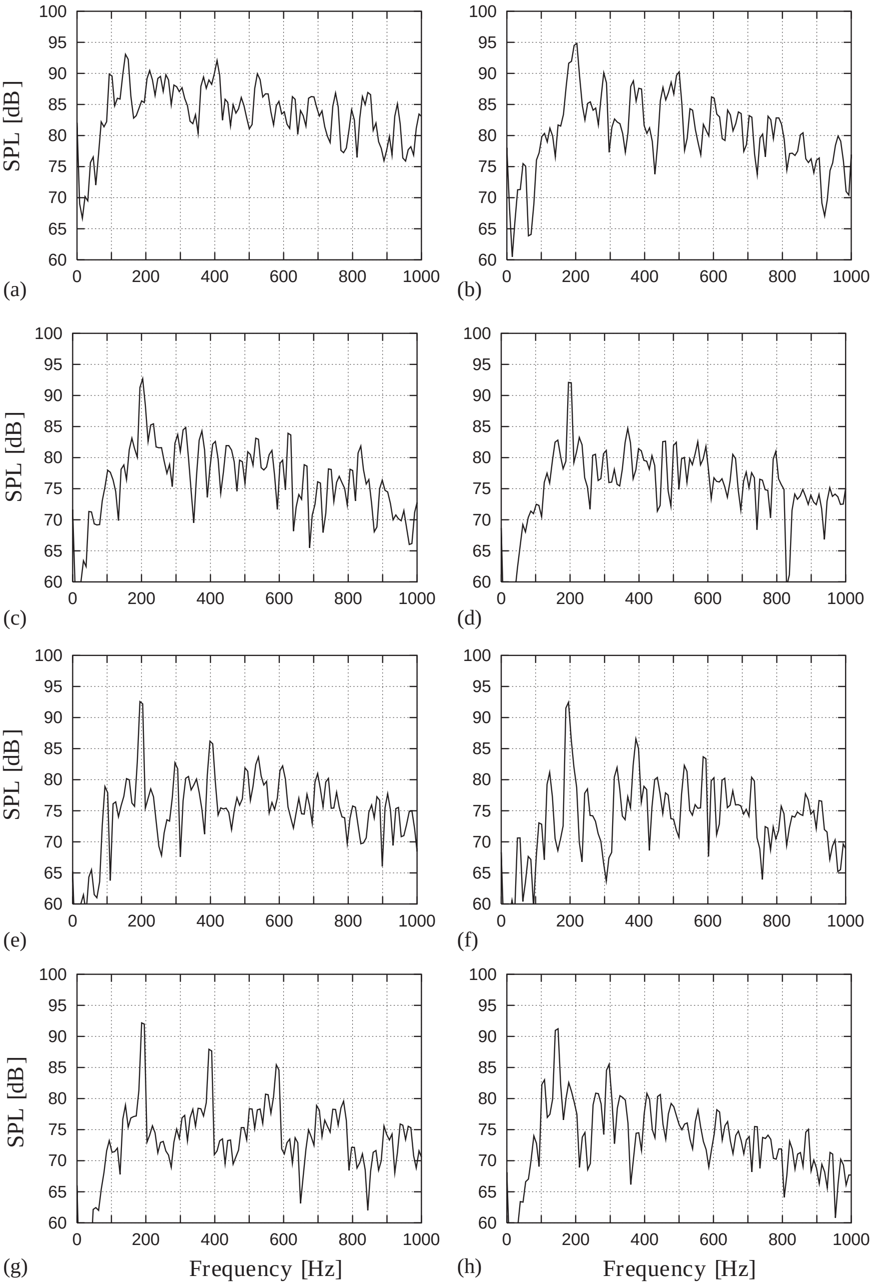

Fig. 9. Influence of the smoothing parameter ε on the sound pressure level (in dB; reference pressure $p_{\mathrm{ref}} = 2 \times 10^{-5}\,\mathrm{N\,m^{-2}}$) at the position $(x, r) = (0.5, 5)d_0$. Single precision calculations (7 digits). (a) $\varepsilon = 0.025d_0$; (b) $\varepsilon = 0.05d_0$; (c) $\varepsilon = 0.1d_0$; (d) $\varepsilon = 0.11d_0$; (e) $\varepsilon = 0.115d_0$; (f) $\varepsilon = 0.12d_0$; (g) $\varepsilon = 0.125d_0$; (h) $\varepsilon = 0.13d_0$.

Table 1
Characteristic frequency f for various values of the smoothing parameter ε

ε/d_0	0.025	0.05	0.1	0.11	0.115	0.12	0.125	0.13
f (Hz)	140.7	203.3	203.3	203.3	195.5	195.5	187.6	148.6

hydrodynamic pressure level at two locations on the end plate, Fig. 12 at the edge of the hole and Fig. 13 about midway between the edge of the hole and the outer edge. These spectra are similar to the sound pressure spectra shown in Fig. 9, particularly for $\varepsilon \geqslant 0.115d_0$. Figs. 14 and 15 show the velocity fluctuation level at two locations in the shear layer; Fig. 14 at $(x, r) = (0.5, 0.5)d_0$, midway between nozzle exit and end plate, and Fig. 15 at $(x, r) = (0.9, 0.5)d_0$, near the end plate. The zero component in these spectra is due to a slow drift in the mean values of the velocities. Time histories of the non-dimensional velocity $(u_x - u_0)/u_0$ at the two locations are shown in Fig. 16.

The ‘artificial viscosity’ introduced by increasing ε is seen to reduce the broad-band noise level of the pressure fluctuations on the end plate (Figs. 12 and 13) but to a smaller extent than by the sound (Fig. 9). The velocity fluctuations in the shear layer are only weakly influenced by changes in ε (Figs. 14 and 15) but a ‘too large’ value ($\geqslant 0.13d_0$) changes the characteristic frequency.

7.1.2. *Influence of machine precision*

The computations presented sofar were carried out in single precision (7 digits). To investigate the effect of the machine precision, three cases ($\varepsilon = 0.05d_0$, $0.1d_0$, $0.125d_0$) were recalculated using double precision (15 digits). The results are shown in Fig. 17. Comparison with Fig. 9 shows that the location (value) of the characteristic frequency f is not affected. For $\varepsilon = 0.05d_0$ the peak at f is lower by the double precision calculation. There are no significant differences for $\varepsilon = 0.1d_0$ and $0.125d_0$. As to higher (second and third) harmonics, these are ‘sharper’ by the double-precision calculation for $0.1d_0$, but basically ‘wiped out’ by the double-precision calculation for $0.125d_0$. As to the vortex convection velocities there are no significant differences for any of the three ε values. The calculation for $\varepsilon = 0.125d_0$ was also repeated using the Fujitsu Fortran 90 compiler’s quadruple precision (29 digits). The result is shown in Fig. 22 (Section 7.2). It will be seen that there is basically no difference between this solution and the one obtained in double precision.

From this point onwards the smoothing parameter ε will be prescribed to the value $0.125d_0$. The reasons for this choice are that this gives (i) the most uniform vortex convection velocity u_c (Figs. 10 and 17), (ii) a mean value of u_c that agrees well with values found in the literature (see also Fig. 11), and (iii) a relatively low broad-band noise level and a clear and distinct characteristic frequency f.

7.1.3. *Influence of time-step*

As one vortex ring is released from the nozzle at each time-step Δt, a change in Δt corresponds effectively to a change in the discretization of the shear layer, that is, a chance in the spacing between consecutive vortex rings.

The results presented in Fig. 18 were obtained using fourth-order Runge–Kutta integration and double precision. Doubling the basic time-step (to $\Delta t = 0.05d_0/u_0$) results in a significant

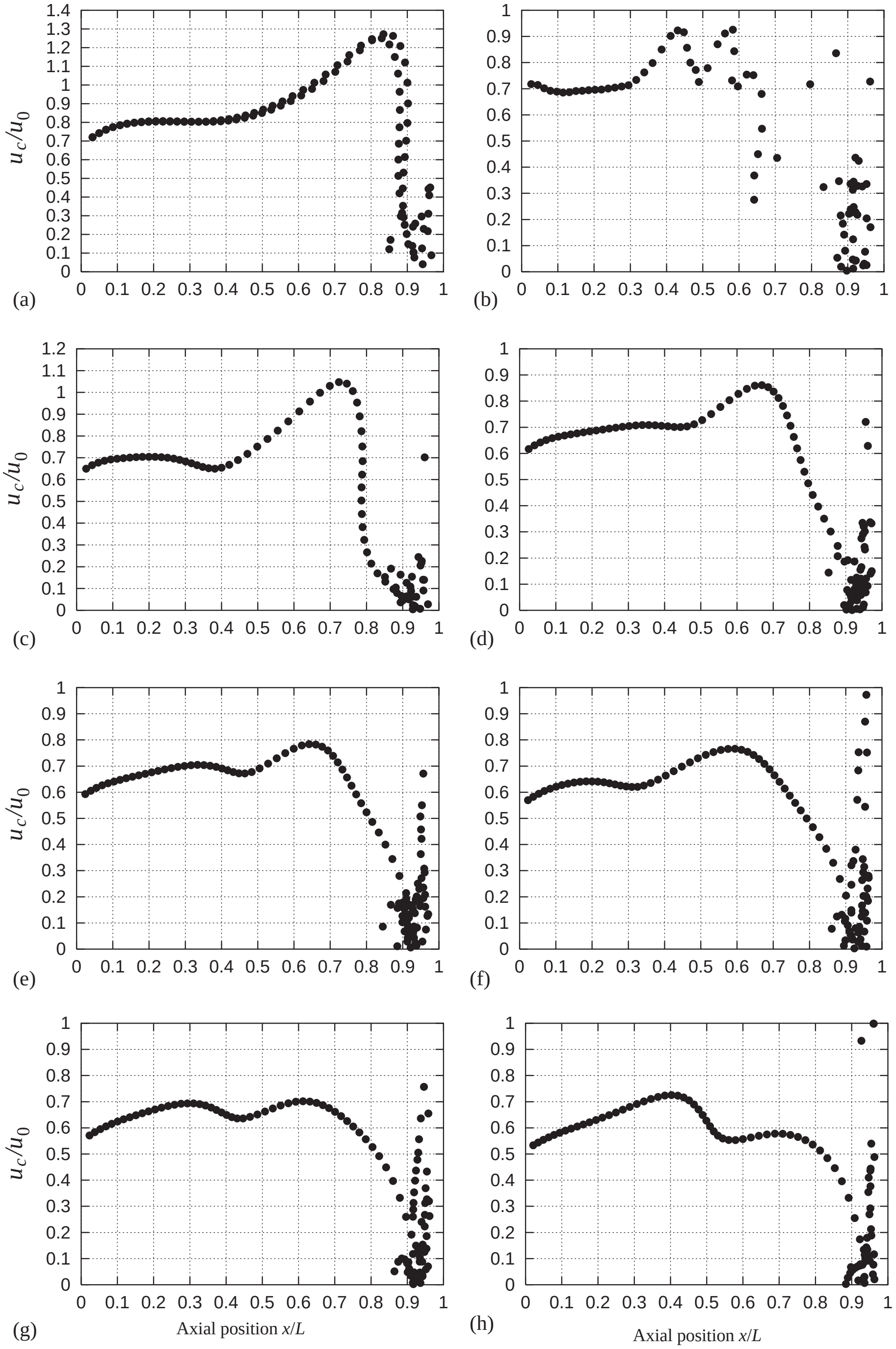

Fig. 10. Influence of the smoothing parameter ε on the vortex convection velocity. Single precision calculations. (a) $\varepsilon = 0.025d_0$; (b) $\varepsilon = 0.05d_0$; (c) $\varepsilon = 0.1d_0$; (d) $\varepsilon = 0.11d_0$; (e) $\varepsilon = 0.115d_0$; (f) $\varepsilon = 0.12d_0$; (g) $\varepsilon = 0.125d_0$; (h) $\varepsilon = 0.13d_0$.

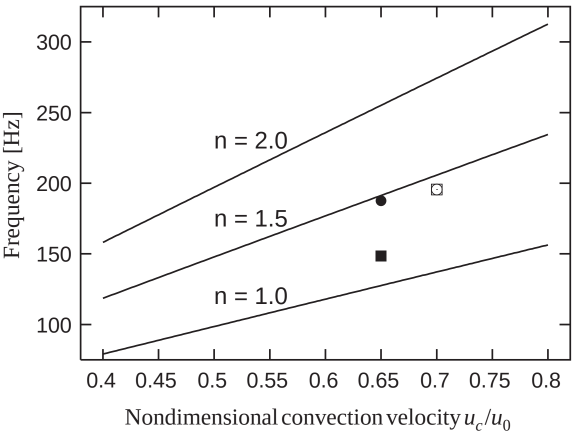

Fig. 11. The hole-tone frequency f as function of the non-dimensional convection velocity u_c/u_0, for three different mode numbers n, in terms of the function $f = (1/u_c + 1/c_0)^{-1} n/L$. Values obtained from numerical simulations: ⊙, $\varepsilon = 0.115d_0$; ▣ , $\varepsilon = 0.12d_0$; ●, $\varepsilon = 0.125d_0$; ■, $\varepsilon = 0.13d_0$.

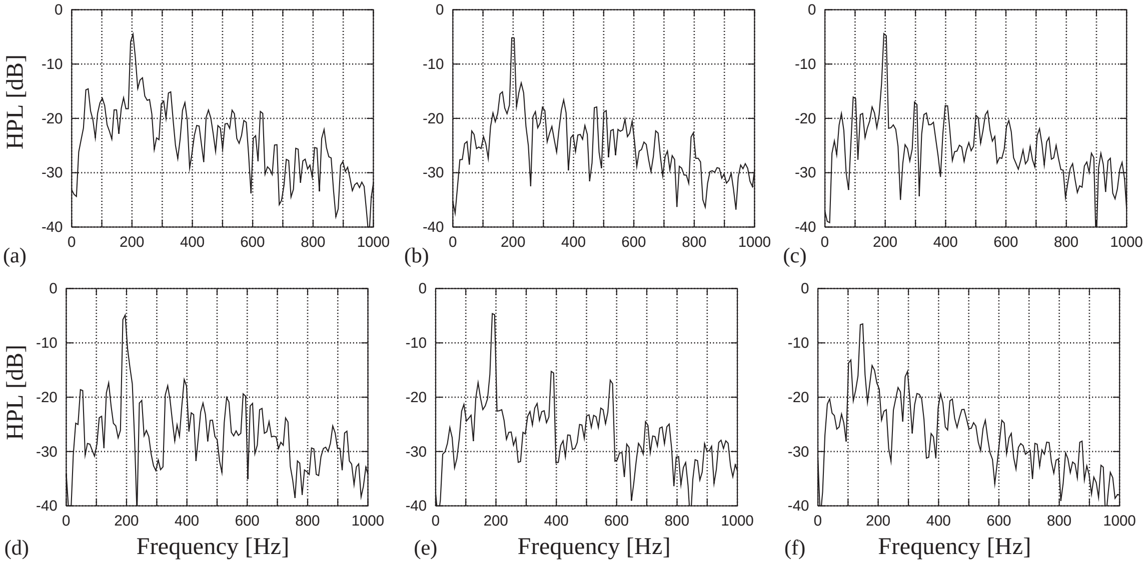

Fig. 12. Influence of the smoothing parameter ε on the hydrodynamic pressure level (in dB; reference pressure $p_{\text{ref}} = \frac{1}{2}\rho_0 u_0^2$) at the position $(x, r) = (1.0, 0.5)d_0$, that is, at the edge of the hole in the end plate. Single precision calculations. (a) $\varepsilon = 0.1d_0$; (b) $\varepsilon = 0.11d_0$; (c) $\varepsilon = 0.115d_0$; (d) $\varepsilon = 0.12d_0$; (e) $\varepsilon = 0.125d_0$; (f) $\varepsilon = 0.13d_0$.

reduction of the peak noise level at the characteristic frequency (part a). Furthermore, the vortex convection velocity is reduced, to an average value of $\sim 0.55u_0$ (part b). Halving the basic time-step (to $\Delta t = 0.0125d_0/u_0$) results in a more clear appearance of the higher harmonics of the characteristic frequency f (part c), but the basic value of f is unaffected, as is the vortex

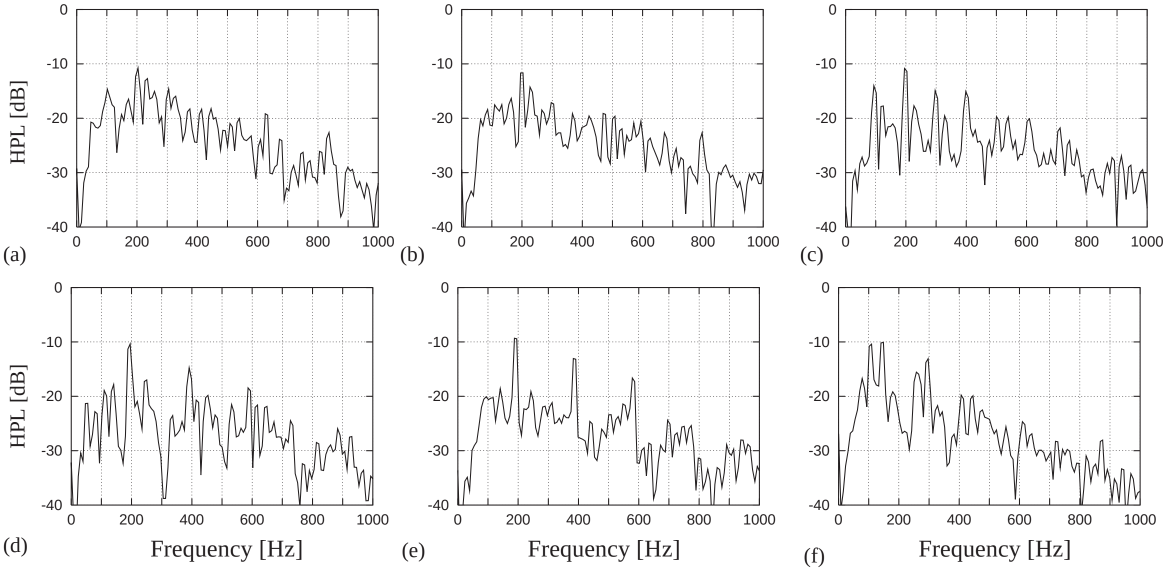

Fig. 13. Influence of the smoothing parameter ε on the hydrodynamic pressure level (in dB; reference pressure $p_{\mathrm{ref}} = \frac{1}{2}\rho_0 u_0^2$) at the position $(x, r) = (1.0, 1.5)d_0$. This is about midway between the outer edge and the edge of the hole in the end plate. Single precision calculations. (a) $\varepsilon = 0.1d_0$; (b) $\varepsilon = 0.11d_0$; (c) $\varepsilon = 0.115d_0$; (d) $\varepsilon = 0.12d_0$; (e) $\varepsilon = 0.125d_0$; (f) $\varepsilon = 0.13d_0$.

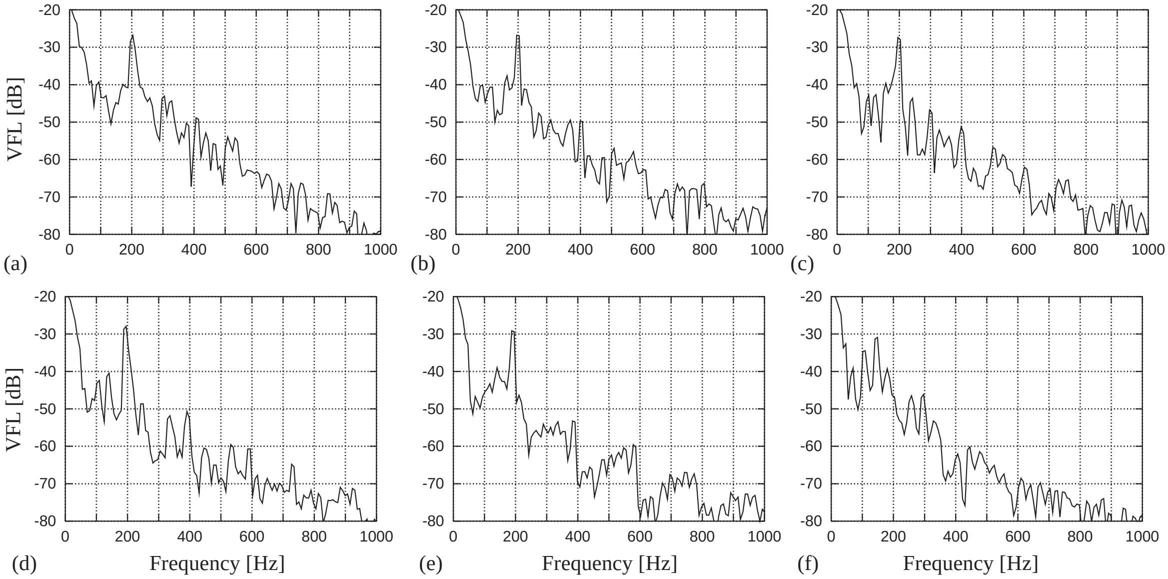

Fig. 14. Influence of the smoothing parameter ε on the velocity fluctuation level (in dB; reference velocity u_0) at the position $(x, r) = (0.5, 0.5)d_0$, that is, in the shear layer, midway between the nozzle exit and the end plate. Single precision calculations. (a) $\varepsilon = 0.1d_0$; (b) $\varepsilon = 0.11d_0$; (c) $\varepsilon = 0.115d_0$; (d) $\varepsilon = 0.12d_0$; (e) $\varepsilon = 0.125d_0$; (f) $\varepsilon = 0.13d_0$.

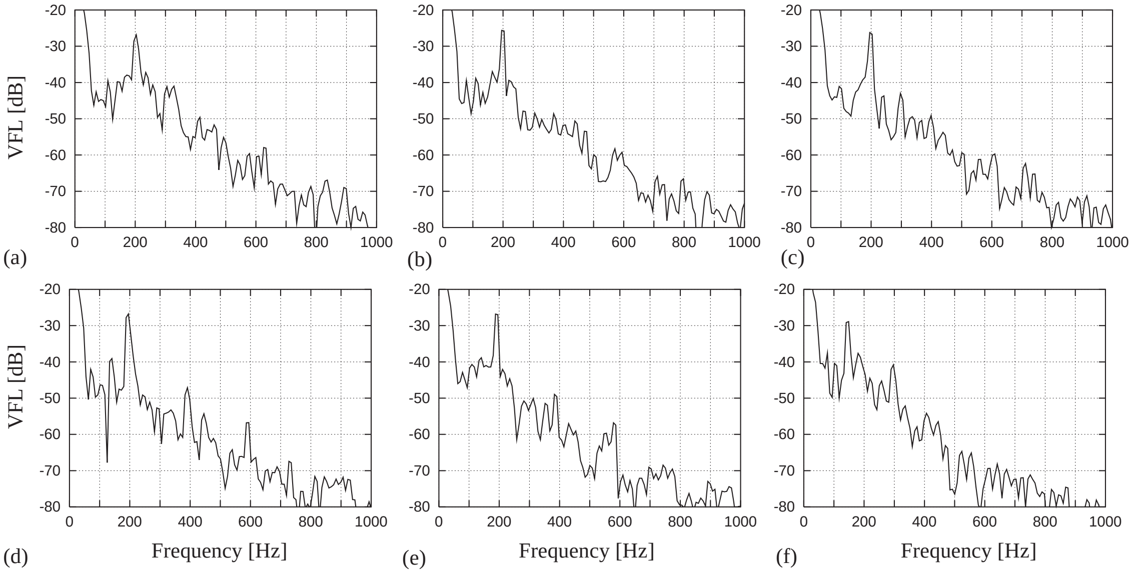

Fig. 15. Influence of the smoothing parameter ε on the velocity fluctuation level (in dB; reference velocity u_0) at the position $(x, r) = (0.9, 0.5)d_0$, that is, in the shear layer, close to the end plate. Single precision calculations. (a) $\varepsilon = 0.1d_0$; (b) $\varepsilon = 0.11d_0$; (c) $\varepsilon = 0.115d_0$; (d) $\varepsilon = 0.12d_0$; (e) $\varepsilon = 0.125d_0$; (f) $\varepsilon = 0.13d_0$.

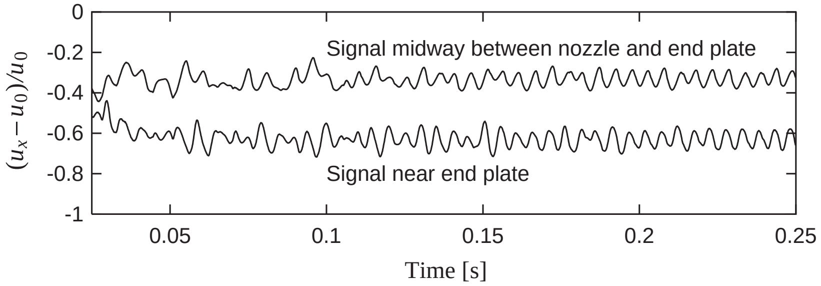

Fig. 16. Time history of the fluctuating axial velocity in the shear layer, at two different locations.

convection velocity (part d). Comparing the results of Figs. 17 and 18, and weighing the gain in accuracy with the increase in computation time, it is decided to use the time-step $\Delta t = 0.025d_0/u_0$ in the calculations to follow.

7.1.4. *Influence of integration method*

The first-order Euler method is often used—and considered sufficiently accurate—for updating the positions of discrete vortices, e.g. [19,40]. The results shown in Fig. 19 were calculated using this method, and single precision. The calculations were repeated in double precision, but in this case extended machine precision has no appreciable influence. Comparing with the previous results (obtained using the fourth-order Runge–Kutta method) it is seen that the Euler

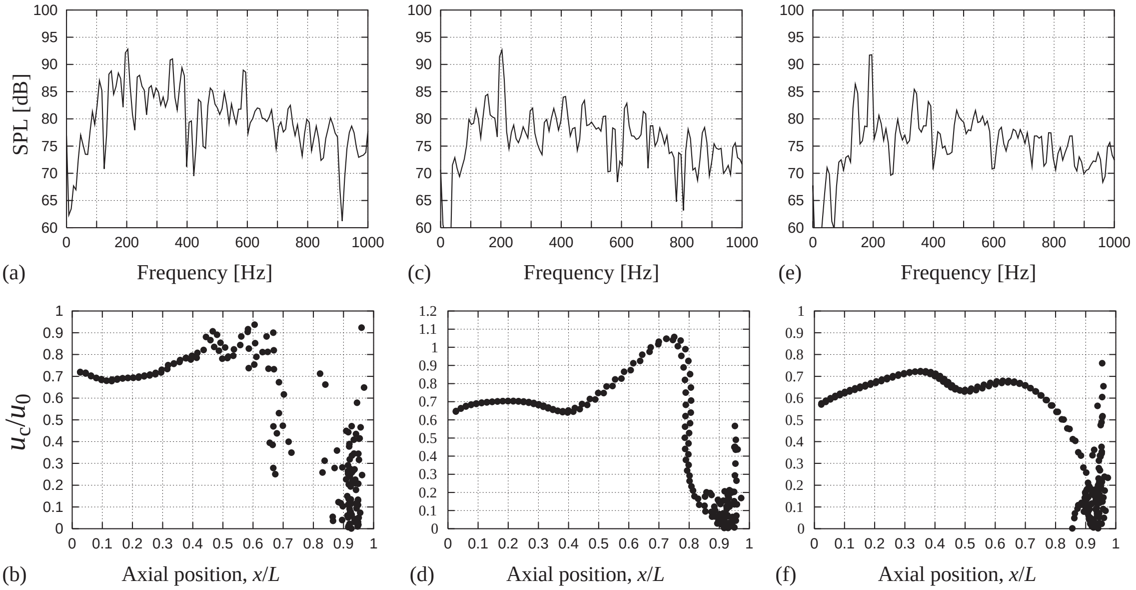

Fig. 17. Computations with double precision (15 digits). (a) Sound pressure level, (in dB; reference pressure $p_{\mathrm{ref}} = 2 \times 10^{-5}\,\mathrm{N\,m^{-2}}$) at the position $(x, r) = (0.5, 5)d_0$, for $\varepsilon = 0.05d_0$. (b) Corresponding vortex convection velocity. (c) Sound pressure level for $\varepsilon = 0.1d_0$. (d) Corresponding vortex convection velocity. (e) Sound pressure level for $\varepsilon = 0.125d_0$. (f) Corresponding vortex convection velocity.

method gives a little lower hole-tone frequency f, and a strong weakening of the higher harmonics.

7.1.5. Influence of forced acoustic excitation

As a preliminary to the influence of acoustic feedback, this section considers the influence of forced acoustic excitation, as described in Section 5. The forcing frequency f_d is prescribed as 200 Hz ($\sim f$), and the influence distance x_{id} as $0.2d_0$ (see Eq. (52)), that is, the excitation acts in the domain $0 \leqslant x \leqslant 0.2d_0$. [This value was chosen in accordance with the experimental setup, see Section 8.1.] Three velocity amplitudes are considered, namely $A_d = 0.01, 0.05$ and 0.1. The effective forcing amplitude of the velocity perturbations, $v_{\max}$ say, which takes into account the effect of the finite time step, may be estimated as follows [40]. Rewriting the last of the expressions in Eq. (52) as $r_i := r_i + \Delta r$, (53) gives $\Delta r = A_d u_0 \cos(2\pi f_d t)\Delta t$. Then $v_{\max} = (\mathrm{d}\Delta r/\mathrm{d}t)_{\max} = 2\pi f_d A_d u_0 \Delta t$. Inserting $f_d = 200\,\mathrm{Hz}$ and $\Delta t = 0.025 d_0/u_0$ gives $v_{\max} = \frac{\pi}{2} A_d$ [m/s]. With the three excitation levels $A_d = 0.01, 0.05$, and 0.1, the velocity ratio $v_{\max}/u_0$ takes the values 0.001571, 0.007854, and 0.01571, or equivalently, 0.1571%, 0.7854%, and 1.571%, respectively. These values are comparable with the forcing levels used in experiments (typically 0.2%–2%, see Refs. [41,42], and references therein).

The influence of the forcing on the sound pressure level at the position $(x, r) = (0.5, 5)d_0$ is shown in Fig. 20. Calculations are performed in both single precision (parts a–f) and double precision (parts g–l), using both fourth-order Runge–Kutta integration (parts a–c and g–i) and first-order Euler integration (parts d–f and j–l). For the single precision calculations with

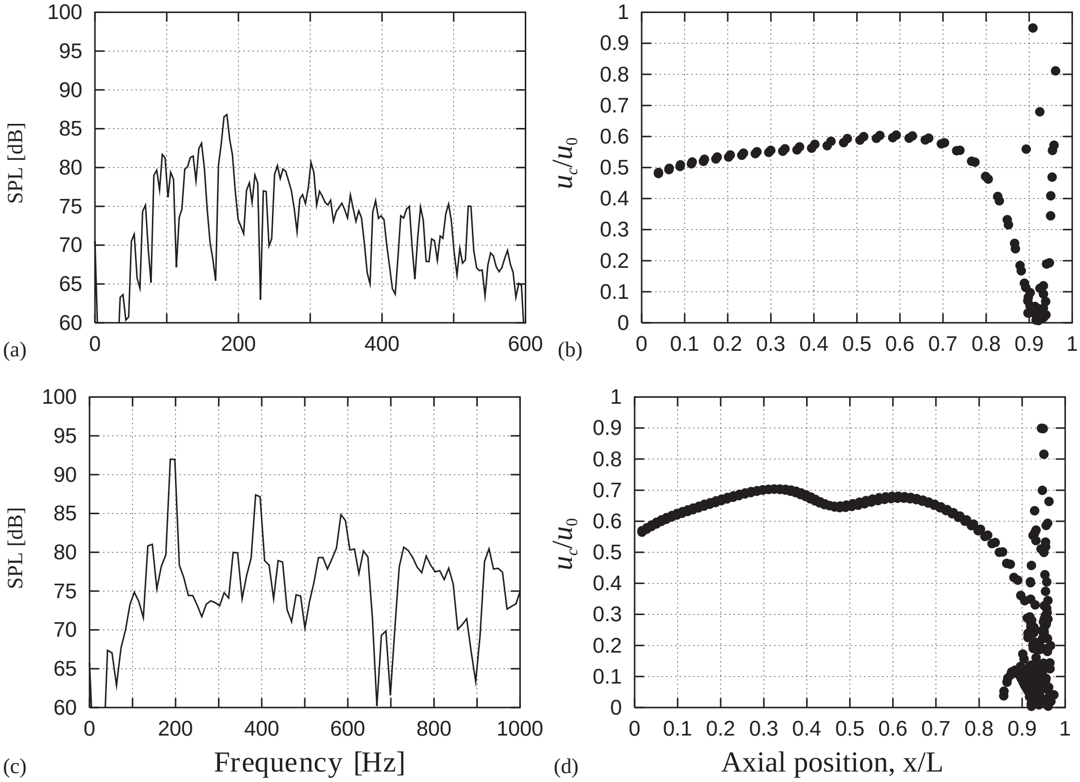

Fig. 18. Influence of time step. [The smoothing parameter $\varepsilon = 0.125d_0$, and double precision is used.] (a) Sound pressure level, (in dB; reference pressure $p_{\text{ref}} = 2 \times 10^{-5}\,\text{N}\,\text{m}^{-2}$) at the position $(x, r) = (0.5, 5)d_0$, for $\Delta t = 0.05d_0/u_0$. (b) Corresponding vortex convection velocity. (c) Sound pressure level for $\Delta t = 0.0125d_0/u_0$. (d) Corresponding vortex convection velocity.

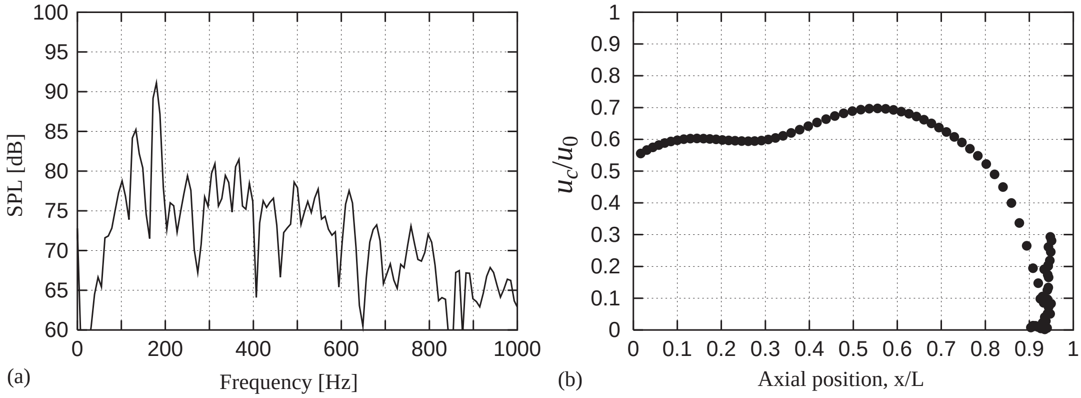

Fig. 19. Influence of integration method; time integration by the Euler method (in single precision). (a) Sound pressure level, (in dB; reference pressure $p_{\text{ref}} = 2 \times 10^{-5}\,\text{N}\,\text{m}^{-2}$) at the position $(x, r) = (0.5, 5)d_0$, for $\varepsilon = 0.125d_0$. (b) Corresponding vortex convection velocity.

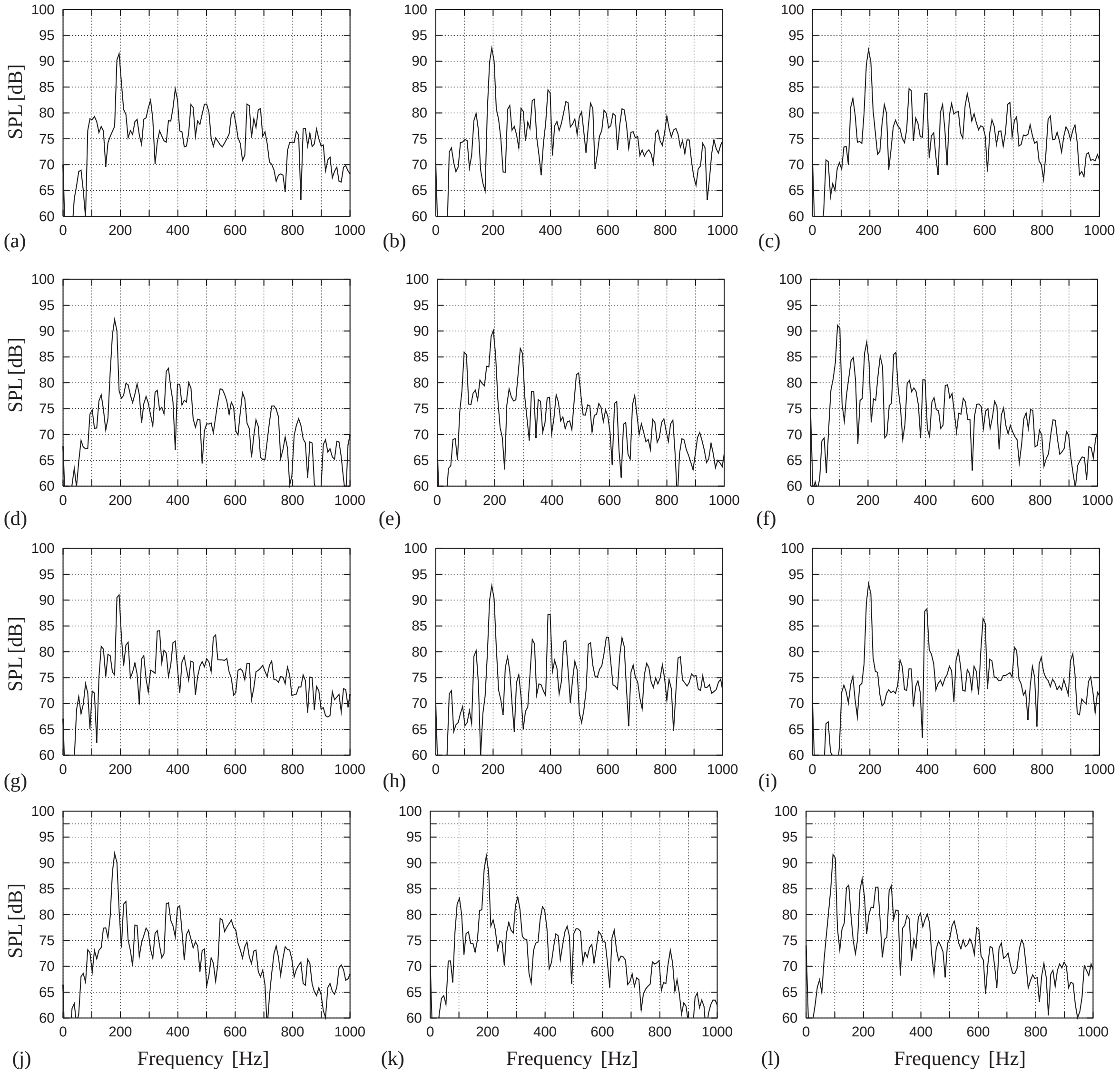

Fig. 20. Influence of forced excitation on the sound pressure level (in dB; reference pressure $p_{\mathrm{ref}} = 2 \times 10^{-5}\,\mathrm{N\,m^{-2}}$) at the position $(x, r) = (0.5, 5)d_0$ (for $\varepsilon = 0.125d_0$). The forcing frequency $f = 200\,\mathrm{Hz}$. Parts (a–f) are single precision calculations (7 digits); parts (g–l) are double precision (15 digits). (a,g) Excitation amplitude $A = 0.01u_0$, integration by the fourth-order Runge–Kutta (RK) method; (b,h) $A = 0.05u_0$, RK integration; (c,i) $A = 0.1u_0$, RK integration; (d,j) $A = 0.01u_0$, integration by the first-order Euler (E) method; (e,k) $A = 0.05u_0$, E integration; (f,l) $A = 0.1u_0$, E integration.

Runge–Kutta time-integration (parts a–c) the acoustic excitation destroys the sharp sub-harmonics (compare with Fig. 9g) but does not affect the characteristic hole-tone frequency for any of the three amplitude levels. Considering next the calculations with Euler time-integration (parts d–f), the acoustic spectrum is unaffected by the excitation with $A_d = 0.01$ but respond markedly different from the previous results by the excitations with $A_d = 0.05$ and 0.1. By $A_d = 0.05$ the subharmonic $\frac{1}{2}f_0$ is excited, together with the combinations $\frac{1}{2}f_d + f_d$ and $\frac{1}{2}f_d + 2f_d$. By $A_d = 0.1$ the subharmonic $\frac{1}{2}f_d$ comes out very strongly, 'taking over' from f. The combination $\frac{1}{2}(\frac{1}{2}f_d + f_d)$ is also distinct, as is any combination of the three just mentioned frequencies.

In contrast to the single precision calculations, the acoustic excitation *reinforces* the subharmonics of f_d by the double precision calculations with Runge–Kutta time-integration (parts g–i), and they come out very strongly at the most powerful excitation. The double precision calculations with Euler time-integration (parts j–l) are, on the other hand, virtually identical to the single precision calculations.

The forced excitation results give some important indications concerning the numerical representation of the acoustic feedback. It is evident that first-order Euler integration and single precision computations are sufficient to represent the hydrodynamic behavior of the vortex system. But the Euler integration is not accurate enough to trace the effect of acoustic disturbances to the vortices. The integration error by far overshadows the roundoff errors in single precision, so nothing is gained by going to double precision. In the case of the fourth-order Runge–Kutta integration, higher machine precision has a clear influence on the representation of the higher harmonics of the characteristic frequency.

7.2. Computations with acoustic feedback

As in the previous forced excitation examples the influence distance x_{id} of the acoustic feedback is specified as $0.2d_0$. [It was initially thought that only the latest released vortex ring should be disturbed. In this way each vortex ring receives a velocity perturbation one time only during its 'life'. This turned out to have too little effect, and a finite influence domain was chosen.] In the light of the forced excitation results the calculations will be done in, at least, double precision, with time-integration by the fourth-order Runge–Kutta method.

A time series for the acoustic velocity feedback due to the dipole pressure (41) is shown in Fig. 21. The amplitude of the radial component v_r is approximately $0.025u_0$ while the axial component v_x is very small. [The magnitude of v_x will be greatly increased by a smaller hole in the end plate.] The amplitude of v_r is comparable with the values considered by forced excitation in

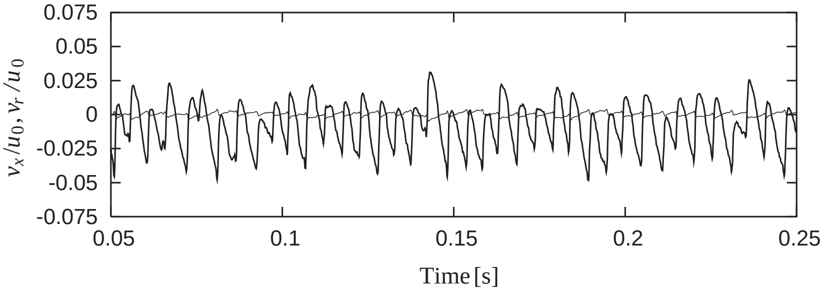

Fig. 21. Acoustic feedback velocities (double precision calculation). The velocity with largest amplitude is v_r; the one with smallest amplitude is v_x.

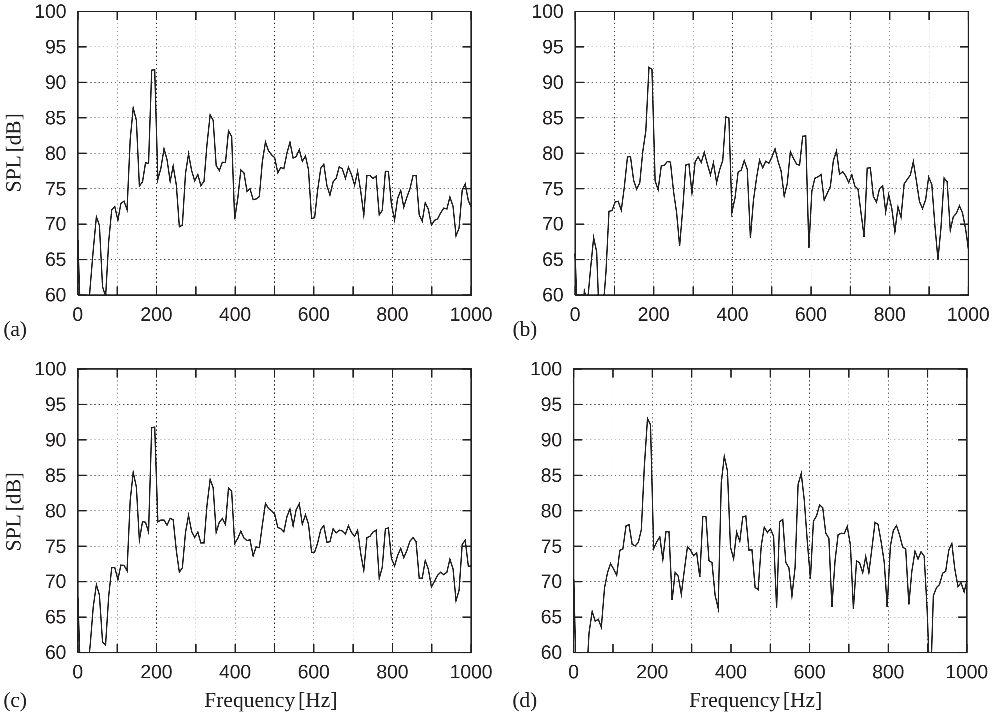

Fig. 22. Influence of acoustic feedback on the sound pressure level (in dB; reference pressure $p_{\mathrm{ref}} = 2 \times 10^{-5}\,\mathrm{N\,m^{-2}}$) at the position $(x, r) = (0.5, 5)d_0$. [Time integration by fourth-order Runge–Kutta method. Smoothing parameter $\varepsilon = 0.125d_0$.] (a) No feedback, double precision (15 digits). (b) Feedback, double precision. (c) No feedback, quadruple precision (29 digits). (d) Feedback, quadruple precision.

the previous subsection. Using the method outlined there the forcing amplitude of the velocity perturbations is, with $u_0 = 10\,\mathrm{m/s}$, estimated as $v_{\max} \approx 0.03927\,\mathrm{m/s}$. To check the order of magnitude of this result it may be useful to apply the far-field approximation for the acoustic particle velocity, v_a say, corresponding to an acoustic pressure p, which is obtained as $v_a = p/(\rho c_0)$ [32]. Setting $v_a = 0.03927\,\mathrm{m/s}$, this corresponds to a pressure amplitude $\sim 16\,\mathrm{Pa}$, or a sound $\sim 118\,\mathrm{dB}$. This is a quite loud sound, but it appears reasonable as the feedback works in the acoustic near-field, very close to the unstable shear layer. It also agrees well with Fig. 8(b). [A pressure amplitude of $0.26 \times \frac{1}{2}\rho_0 u_0^2$ corresponds to 118 dB.] The acoustic velocity feedback (51) due to the monopole pressure was, in comparison, found to be negligibly small. This can also be understood from Fig. 8.

Fig. 22 illustrates the effect of acoustic feedback on the sound spectrum at the position $(x, r) = (0.5, 5)d_0$. Parts (a) and (c) are the results without feedback; parts (b) and (d) are the results with feedback. Parts (a) and (b) are obtained with double precision, parts (c) and (d) with quadruple precision. It is seen that *the effect of the feedback is to suppress the broad-band noise and reinforce the characteristic frequency f and its higher harmonics*. The level of f itself is not significantly affected, but the levels of the higher harmonics are significantly raised. As discussed in the previous subsection, the representation of the higher harmonics is sensitive to roundoff errors, as the peaks at these frequencies clearly are higher by the quadruple precision calculation. The sub-harmonic components $\frac{1}{4}f \approx 50\,\mathrm{Hz}$ and $\frac{1}{4}f + \frac{1}{2}f \approx 150\,\mathrm{Hz}$ are also suppressed by the acoustic feedback.

8. Comparison with experiment

Prior to the present theoretical/numerical work a number of experiments have been carried out by the second author (M.N.) at Yamagata University. In the following a brief discussion of the experimental equipment is given, and calculated results are compared with experimental data.

8.1. Description of experimental equipment

The experimental equipment is sketched in Fig. 23. The dimensions are as given in Section 6.1, with the single exception of the outer shape of the end plate. While it is necessary to assume a

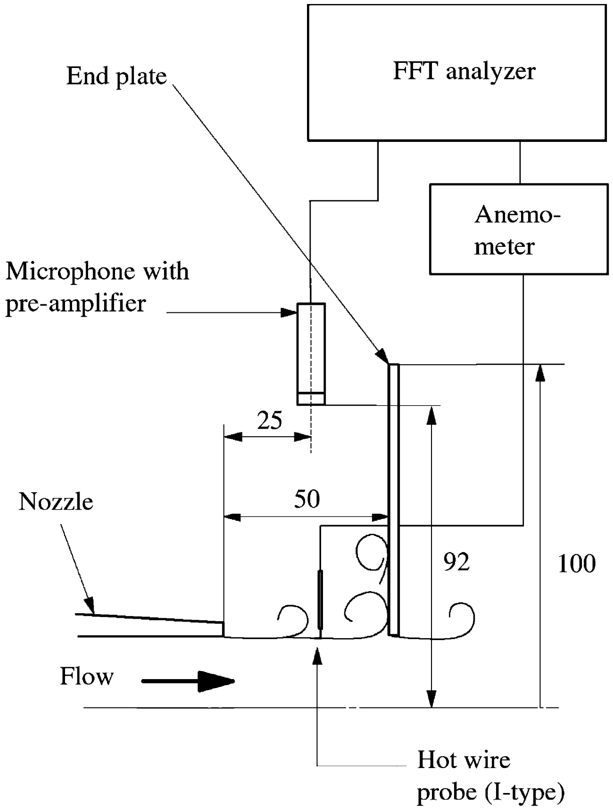

Fig. 23. Schematic illustration of the experimental set-up.

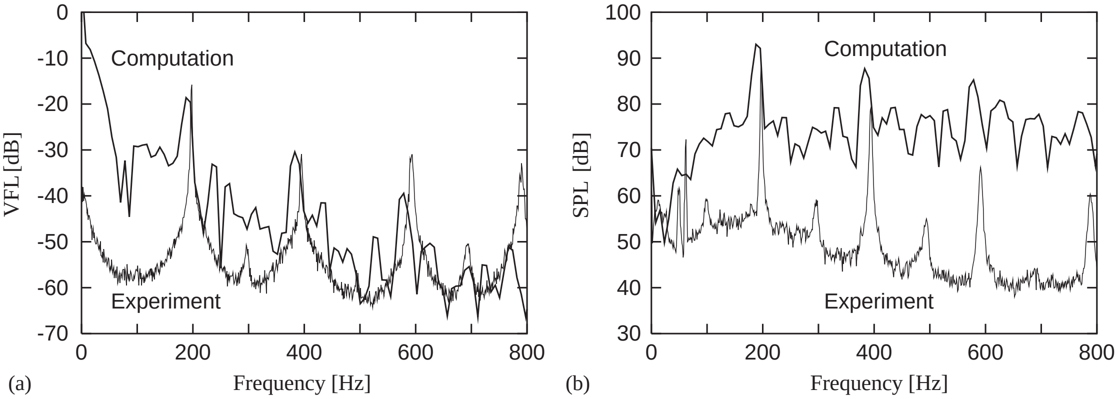

Fig. 24. Comparison between computed and experimental frequency spectra. (a) Velocity fluctuation level (VFL) in the shear layer, midway between nozzle and end plate. (b) Qualitative comparison between computed and experimental sound pressure levels. [The experimental spectrum is for the position $(x, r) = (0.5, 1.84)d_0$ while the computed one is for the position $(x, r) = (0.5, 5)d_0$, so the magnitude of the peaks are not to be compared, only the qualitative features.]

disc-shaped end plate in the theory, the experimental end plate is actually rectangular, with dimensions 200 mm (height) × 270 mm (width). [As mentioned before, the diameter of the computational plate was chosen as 250 mm, a little more than the average $\{(200 + 270)/2\}$ mm.]

Air from a centrifugal blower goes through a ~ 160 mm long mouthpiece before leaving the nozzle. Fluctuating flow velocities are measured by a Dantec I-type hot-wire probe, and sound pressure levels by a condenser microphone (Ono Sokki MI-1232). Data are passed through an anemometer (Dantec 56C01 CTA) and a microphone preamplifier (Ono Sokki MI-3220), respectively, to an Ono Sokki CF-5220 multi-purpose FFT analyzer.

The hole-tone setup is also equipped with an apparatus for forced acoustic excitation of the jet near the nozzle exit, consisting of a chamber with a loudspeaker and an excitation nozzle (not shown in Fig. 23). The influence domain of the excitation jet was estimated to be ~ 1 cm $\sim 0.2d_0$, as mentioned in Section 7.1.5. [Experiments with forced excitation will however not be considered here.]

The photograph shown in Fig. 1 is from a video sequence, recorded with a high-speed video camera (Fastcam Ultimate, 4500 frames/s). The vortex roll-up is visualized by use of the smoke-wire pulse method.

As in the previous examples the mean flow speed $u_0 = 10$ m/s and the gap length $L = d_0 = 50$ mm, unless stated otherwise.

8.2. Comparison between theory and experiment

Velocity fluctuation levels in the shear layer (in dB, reference 5 m/s (which corresponds to 1 V)), measured at $(x, r) = (0.6, 0.5)d_0$, are shown in Fig. 24(a). It is seen that there is good agreement between the experimental and computational hole-tone frequency f, and also the second harmonic $2f$, both with respect to location and peak level. The agreement is not so good for the

Table 2
Comparison between experimental and computational values of frequencies and peaks of the velocity fluctuation spectrum at $(x, r) = (0.6, 0.5)d_0$, shown in Fig. 24(a)

n		1	2	3	4
f_n (Hz)	Experimental	198	395	594	790
	Computational	188	383	579	766
VFL_n (dB)	Experimental	−15.8	−30.9	−31.0	−32.9
	Computational	−18.6	−30.4	−39.4	−51.2

third and fourth harmonics of f. The numerical values of frequencies and peaks are summarized in Table 2.

Fig. 24(b) shows experimental and computational sound pressure levels. The experimental spectrum was recorded at the position $(x, r) = (0.5, 1.8)d_0$. It must be noticed that this position is in the very near-field, well *within* the outer edge of the end plate. Computation of the sound pressure here is very difficult, as discussed at the end of Section 3. The computational spectrum in Fig. 24(b) is thus not recorded at $(x, r) = (0.5, 1.8)d_0$, but at $(x, r) = (0.5, 5)d_0$ as in the previous examples. The two spectra can therefore be compared quantitatively with respect to frequencies but only qualitatively with respect to peak levels. The frequencies are seen to agree well but, on the contrary to part (a), the levels of the higher harmonics appear here to be, relatively, too high. It must also be remarked that the broad-band noise levels of the computations are significantly higher that the experimental ones. This may be explained by the random (chaotic) motions of individual vortices [39] which however are damped by the ‘artificial viscosity’, expressed by the parameter ε.

The characteristic frequency f is shown as function of jet speed u_0 in Fig. 25(a). The full lines depict (1), drawn with $u_c = 0.65u_0$, as estimated in Section 7.1.1. The experimental results (open dots) display a complicated pattern of mode-jumping. For $5.0\,\mathrm{m/s} \leqslant u_0 \leqslant 9.0\,\mathrm{m/s}$ they follow the $n = 2.5$ line, and for $9.0\,\mathrm{m/s} \leqslant u_0 \leqslant 14.8\,\mathrm{m/s}$ the $n = 1.5$ line. But frequencies following the $n = 3.0$ line are also present in the range $12.0\,\mathrm{m/s} \leqslant u_0 \leqslant 14.8\,\mathrm{m/s}$. The line $n = 4.0$ is followed in the range $14.8\,\mathrm{m/s} \leqslant u_0 \leqslant 19.0\,\mathrm{m/s}$. The last data point, for $u_0 = 20.0\,\mathrm{m/s}$, lyes on the $n = 3.0$ line. The simulation results (solid dots) all follow the $n = 1.5$ line. Here it is remarked that in the experiment the velocity $u_0 = 10\,\mathrm{m/s}$, which corresponds to a Strouhal number $fL/u_0 \sim 1.0$, gives the most distinct characteristic frequency and the loudest sound. This may indicate that $n = 1.5$ is the ‘preferred’ mode for the considered geometry, and may give a hint to why the computations ‘hinge’ to this mode. But it must be emphasized that more work is needed in order to understand the mechanism behind the mode jumps.

Fig. 25(b) shows the characteristic frequency f as function of the non-dimensional gap length L/d_0. No experimental results are available to check this investigation; it is included anyway in this section because of its relation to Fig. 25(a). As in part (a) the full lines depict (1), drawn with $u_c = 0.65u_0$. Open dots represent calculations with the fourth-order Runge–Kutta method, while solid dots represent calculations with the first-order Euler method. Here mode jumps occur, but

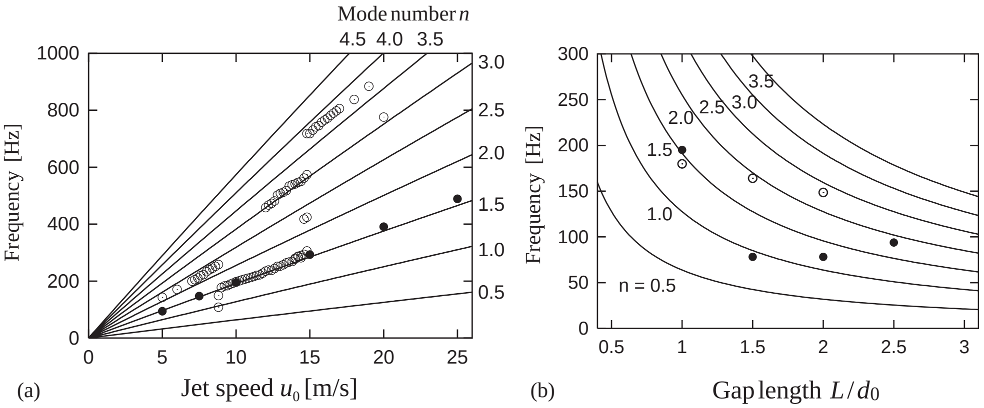

Fig. 25. (a) Variation of hole-tone frequency f_0 with jet speed u_0. —, Eq. (1); •, computation; ○, experiment. (b) Variation of hole-tone frequency f_0 with non-dimensional gap length L/d_0. —, Eq. (1); •, computation with fourth-order Runge–Kutta integration; ○, computation with first-order Euler integration.

the results are highly dependent upon the accuracy of the time integration. It turns out that by increasing the gap length the broadband noise level in the sound spectrum is significantly raised and the characteristic frequency does not come out as distinct as by the small initial gap, $L = d_0$. On the contrary, many components of nearly equal magnitude compete. In this way mode jumps easily occur.

9. Conclusions and discussion

An axisymmetric numerical simulation approach to the hole-tone feedback cycle problem has been presented. It is based on the discrete vortex method, using axisymmetric vortex rings, combined with an acoustic feedback mechanism which is based on Curle's equation. The main findings from the numerical study can be summarized as follows.

1. The simulated shear layer velocity fluctuations are in good agreement with experiments, both with respect to frequencies and amplitude levels. The frequencies of sound pressure fluctuations are also found to agree well with the experimental values. The numerical method is however incapable of providing results for the very near-field where the measurements were made, so sound pressure levels can only be compared qualitatively.
2. The simulated results follow the criterion (1), in agreement with the experimental results. But the simulations lock on to a single value of the mode number n, while the experiments display a complicated pattern of mode jumps.
3. The smoothing (vortex-blob regularization) parameter ε defined in Eq. (3) works as 'artificial viscosity', as it increases the thickness of the shear layer.
4. The smoothing parameter significantly affects the appearance of the rolled-up 'smoke rings', the vortex convection velocity, and the level of broadband noise in sound and velocity

spectra, but the characteristic hole-tone frequency is fairly insensitive to changes in this parameter.

5. The basic feedback cycle works hydrodynamically. In the present context this means that the discrete vortex method alone, without *acoustic* feedback, can predict the fundamental characteristics of the problem.
6. For the geometry considered, where the diameter of the end plate is much smaller than the acoustic wavelength, the produced sound is mainly of dipole type. The effect of the corresponding acoustic feedback is to suppress the broadband noise and reinforce the characteristic hole-tone frequency and its higher harmonics, as dictated by the hydrodynamics.
7. In cases with disturbance of the vortices by forced acoustic excitation or acoustic feedback, high precision computer arithmetics and accurate time integration becomes particularly important.

Following up on item No. 2, we emphasize that more work is needed to understand the mechanism behind mode jumps. Linearized models [14,15] can give the characteristic frequency for any *given* mode number n, but the selection of n may be governed by nonlinear processes. Nonetheless, Brevdo [43] recently suggested a selection criterion based on a linearized model. Considering oscillations with time-dependence $\exp(-\mathrm{i}\omega t)$ it is suggested as a hypothesis that the system will select the mode corresponding to the complex root $\omega_j = \mathrm{Re}(\omega_j) + \mathrm{i}\,\mathrm{Im}(\omega_j)$ of the dispersion function $\mathscr{D}(\omega)$ for which $\mathrm{Im}(\omega_j)$ is largest and thus 'most unstable'.

Finally, following up on item No. 4, the level of broadband noise in the computational frequency spectra is higher than in the experimental ones for any useful value of the smoothing parameter. Many different regularization methods have been proposed (for example vortex patch regularization, viscous regularization, and surface tension; see Ref. [30] for a recent review), and another method than the vortex-blob regularization used here might be more efficient for the present problem. Better suppression of the numerical noise may lead to improved behavior of the numerical scheme with respect to mode jumping, and to a better understanding of this phenomenon. Improved smoothing schemes is thus an important and interesting problem for a future study.

Acknowledgements

We wish to thank Professor Hiromichi Umemiya for his support, Dr. Akira Sato and Mr. Eiji Haga for their technical assistance, and Dr. Erik Lund at Aalborg University (Denmark) for providing the plotting software 'FEPlot'. A number of computations were carried out at Yamagata University Computing Service Center.

Appendix A. Evaluation of the derivatives in Eqs. (2) and (6)

Evaluation of the terms $\partial\Psi/\partial x$, $\partial\Psi/\partial r$, $\partial^2\Psi/\partial x^2$ and $\partial^2\Psi/\partial r^2$, which appear in Eqs. (2) and (6), is shown in this appendix.

A.1. First derivatives

Use of the chain rule on the first of the equations (3) gives

$$\begin{aligned}\frac{\partial\Psi}{\partial x}&=\frac{x-x_v}{\eta_1}\frac{\partial\Psi}{\partial\eta_1}+\frac{x-x_v}{\eta_2}\frac{\partial\Psi}{\partial\eta_2},\\ \frac{\partial\Psi}{\partial r}&=\frac{r-r_v}{\eta_1}\frac{\partial\Psi}{\partial\eta_1}+\frac{r+r_v}{\eta_2}\frac{\partial\Psi}{\partial\eta_2},\end{aligned}\tag{54}$$

where

$$\begin{aligned}\frac{\partial\Psi}{\partial\eta_1}&=\frac{\Gamma}{2\pi}(K-E)+\frac{\Gamma}{2\pi}(\eta_1+\eta_2)\frac{\partial}{\partial\eta_1}(K-E),\\ \frac{\partial\Psi}{\partial\eta_2}&=\frac{\Gamma}{2\pi}(K-E)+\frac{\Gamma}{2\pi}(\eta_1+\eta_2)\frac{\partial}{\partial\eta_2}(K-E).\end{aligned}\tag{55}$$

Here

$$\frac{\partial K}{\partial\eta_1}=\frac{\partial K}{\partial\lambda}\frac{\partial\lambda}{\partial\eta_1},\quad \frac{\partial E}{\partial\eta_1}=\frac{\partial E}{\partial\lambda}\frac{\partial\lambda}{\partial\eta_1},\tag{56}$$

and similar with respect to η_2. The second of the equations (3) gives

$$\frac{\partial\lambda}{\partial\eta_1}=-\frac{1+\lambda}{\eta_1+\eta_2},\quad \frac{\partial\lambda}{\partial\eta_2}=\frac{1-\lambda}{\eta_1+\eta_2}.\tag{57}$$

By making use of Eq. (4) it is found that

$$\frac{\partial K}{\partial\lambda}=\frac{1}{\lambda}\left(\frac{E}{1-\lambda^2}-K\right),\quad \frac{\partial E}{\partial\lambda}=\frac{1}{\lambda}(E-K),\tag{58}$$

and thus,

$$\frac{\partial}{\partial\lambda}(K-E)=\frac{\lambda}{1-\lambda^2}E.\tag{59}$$

Collecting these results, Eq. (55) can be written as

$$\frac{\partial\Psi}{\partial\eta_1}=\frac{\Gamma}{2\pi}\left\{K-\frac{1}{2}\left(1+\frac{\eta_2}{\eta_1}\right)E\right\},\quad \frac{\partial\Psi}{\partial\eta_2}=\frac{\Gamma}{2\pi}\left\{K-\frac{1}{2}\left(1+\frac{\eta_1}{\eta_2}\right)E\right\}.\tag{60}$$

A.2. Second derivatives

Differentiation of Eq. (54) gives

$$\begin{aligned}\frac{\partial^2\Psi}{\partial x^2}=&\frac{1}{\eta_1}\left\{1-\left(\frac{x-x_v}{\eta_1}\right)^2\right\}\frac{\partial\Psi}{\partial\eta_1}+\frac{1}{\eta_2}\left\{1-\left(\frac{x-x_v}{\eta_2}\right)^2\right\}\frac{\partial\Psi}{\partial\eta_2}\\ &+(x-x_v)^2\left\{\frac{1}{\eta_1^2}\frac{\partial^2\Psi}{\partial\eta_1^2}+\frac{1}{\eta_2^2}\frac{\partial^2\Psi}{\partial\eta_2^2}+\frac{2}{\eta_1\eta_2}\frac{\partial^2\Psi}{\partial\eta_1\eta_2}\right\},\end{aligned}$$

$$\frac{\partial^2\Psi}{\partial r^2} = \frac{1}{\eta_1}\left\{1-\left(\frac{r-r_v}{\eta_1}\right)^2\right\}\frac{\partial\Psi}{\partial\eta_1} + \frac{1}{\eta_2}\left\{1-\left(\frac{r+r_v}{\eta_2}\right)^2\right\}\frac{\partial\Psi}{\partial\eta_2}$$
$$+\left(\frac{r-r_v}{\eta_1}\right)^2\frac{\partial^2\Psi}{\partial\eta_1^2} + \left(\frac{r+r_v}{\eta_2^2}\right)^2\frac{\partial^2\Psi}{\partial\eta_2^2} + 2\,\frac{(r-r_v)(r+r_v)}{\eta_1\eta_2}\,\frac{\partial^2\Psi}{\partial\eta_1\eta_2}. \tag{61}$$

Differentiation of Eq. (60) gives, after some algebra,

$$\frac{\partial^2\Psi}{\partial\eta_1^2} = \frac{\Gamma}{2\pi}\left\{-\frac{\eta_2}{\eta_1}\frac{1}{\eta_1+\eta_2}K + \frac{1}{2}\frac{\eta_1+\eta_2}{\eta_1^2}E\right\},$$
$$\frac{\partial^2\Psi}{\partial\eta_2^2} = \frac{\Gamma}{2\pi}\left\{-\frac{\eta_1}{\eta_2}\frac{1}{\eta_1+\eta_2}K + \frac{1}{2}\frac{\eta_1+\eta_2}{\eta_2^2}E\right\},$$
$$\frac{\partial^2\Psi}{\partial\eta_1\eta_2} = \frac{\Gamma}{2\pi}\left\{\frac{1}{\eta_1+\eta_2}K - \frac{1}{2}\frac{\eta_1+\eta_2}{\eta_1\eta_2}E\right\}. \tag{62}$$

Appendix B. Evaluation of the integral in Eq. (37)

Ref. [44] gives the result

$$\int_{-\infty}^{\infty} \mathrm{e}^{\mathrm{i}px} H_0^{(1)}(c\sqrt{b^2-x^2})\,\mathrm{d}x = -\frac{2\mathrm{i}}{\sqrt{c^2+p^2}}\,\mathrm{e}^{\mathrm{i}b\sqrt{c^2+p^2}}, \tag{63}$$

where b, c, and p here are scalar parameters. But an integral on the form $\int_{-\infty}^{\infty} x\,\mathrm{e}^{\mathrm{i}px}H_0^{(1)}(c(b^2-x^2)^{1/2})\,\mathrm{d}x$ appears in Eq. (37). This can be obtained by differentiating Eq. (63) with respect to p, followed by multiplication with $-\mathrm{i}$. This gives the formula

$$\int_{-\infty}^{\infty} x\mathrm{e}^{\mathrm{i}px} H_0^{(1)}(c\sqrt{b^2-x^2})\,\mathrm{d}x = \frac{2p}{c^2+p^2}\left(\frac{1}{\sqrt{c^2+p^2}} - \mathrm{i}b\right)\mathrm{e}^{\mathrm{i}b\sqrt{c^2+p^2}}, \tag{64}$$

by which Eq. (37) is evaluated.

Appendix C. Inversion of the last term in Eq. (45)

To evaluate the inverse Fourier transform of the last term in Eq. (45),

$$\int_{-\infty}^{\infty} \tilde{f}_{xn}\mathrm{e}^{\mathrm{i}D_n\omega/c_0}\,\frac{\mathrm{i}}{\omega}\,\mathrm{e}^{-\mathrm{i}\omega t}\,\mathrm{d}\omega, \tag{65}$$

use can be made of the convolution theorem in form [7, p. 60]

$$\int_{-\infty}^{\infty} \tilde{f}_1(\omega)\tilde{f}_2(\omega)\mathrm{e}^{-\mathrm{i}\omega t}\,\mathrm{d}\omega = \frac{1}{2\pi}\int_{-\infty}^{\infty} f_1(\tau)f_2(t-\tau)\,\mathrm{d}\tau. \tag{66}$$

Eq. (65) can thus be written as

$$\frac{1}{2\pi}\int_{-\infty}^{\infty} f_{xn}(\tau - D_n/c_0)H(t-\tau)\,\mathrm{d}\tau, \tag{67}$$

where $H(t-\tau)$ is the Heaviside unit function, which is zero for $\tau < t$ and unity for $\tau > t$. The final result is

$$\int_{-\infty}^{t} f_{xn}(\tau - D_n/c_0)\,\mathrm{d}\tau. \tag{68}$$

References

[1] Lord Rayleigh, *Theory of Sound*, Vol. II, Dover Publications, New York, 1896, re-issued 1945.

[2] R.C. Chanaud, A. Powell, Some experiments concerning the hole and ring tone, *Journal of the Acoustical Society of America* 37 (1965) 902–911.

[3] M.J. Lighthill, On sound generated aerodynamically. I. General theory, *Proceedings of the Royal Society of London A* 211 (1952) 564–587.

[4] N. Curle, The influence of solid boundaries upon aerodynamic sound, *Proceedings of the Royal Society of London A* 231 (1955) 505–514.

[5] A. Powell, Aerodynamic noise and the plane boundary, *Journal of the Acoustical Society of America* 32 (1960) 982–990.

[6] J.E. Ffowcs Williams, D.L. Hawkings, Sound generation by turbulence and surfaces in arbitrary motion, *Philosophical Transactions of the Royal Society of London A* 264 (1969) 321–342.

[7] M.S. Howe, *Acoustics of Fluid–Structure Interaction*, Cambridge University Press, Cambridge, 1998.

[8] S.J. Hulshoff, A. Hirschberg, G.C.J. Hofmans, Sound production of vortex–nozzle interactions, *Journal of Fluid Mechanics* 439 (2001) 335–352.

[9] J. Anthoine, M. Mettenleiter, O. Repellin, J.-M. Buchlin, S. Candel, Influence of adaptive control on vortex-driven instabilities in a scaled model of solid propellant motors, *Journal of Sound and Vibration* 262 (2003) 1009–1046.

[10] P.C. Kriesels, M.C.A.M. Peters, A. Hirschberg, P.J. Wijnands, High amplitude vortex-induced pulsations in a gas transport system, *Journal of Sound and Vibration* 184 (1995) 343–368.

[11] M.S. Howe, Leaky waves and the production of sound by turbulent flow from an elastic nozzle, *Philosophical Transactions of the Royal Society of London A* 354 (1996) 1–34.

[12] D. Rockwell, E. Naudascher, Self-sustained oscillations of impinging free shear layers, *Annual Review of Fluid Mechanics* 11 (1979) 67–94.

[13] D. Rockwell, Oscillations of impinging shear layers, *AIAA Journal* 21 (1983) 645–664.

[14] D.G. Crighton, The jet edge-tone feedback cycle; linear theory for the operating stages, *Journal of Fluid Mechanics* 234 (1992) 361–391.

[15] M.S. Howe, Edge, cavity and aperture tones at very low Mach numbers, *Journal of Fluid Mechanics* 330 (1997) 61–84.

[16] G.-H. Cottet, P.D. Koumoutsakos, *Vortex Methods: Theory and Practice*, Cambridge University Press, Cambridge, 2000.

[17] S.A.T. Stoneman, K. Hourigan, A.N. Stokes, M.C. Welsh, Resonant sound caused by flow past two plates in tandem in a duct, *Journal of Fluid Mechanics* 192 (1988) 455–484.

[18] M.C. Thompson, K. Hourigan, M.C. Welsh, Acoustic sources in a tripped flow past a resonator tube, *AIAA Journal* 30 (1992) 1484–1491.

[19] J. Katz, A. Plotkin, *Low-Speed Aerodynamics*, Cambridge University Press, Cambridge, 2001.

[20] E. Acton, A modelling of large eddies in an axisymmetric jet, *Journal of Fluid Mechanics* 98 (1980) 1–31.

[21] W.J.A. Dahm, C.E. Frieler, G. Tryggvason, Vortex structure and dynamics in the near field of a coaxial jet, *Journal of Fluid Mechanics* 241 (1992) 371–402.

[22] X. Jing, X. Sun, Discrete vortex simulation on the acoustic nonlinearity of an orifice, *AIAA Journal* 38 (2000) 1565–1572.

[23] B. de Bernardinis, J.M.R. Graham, K.H. Parker, Oscillatory flow around disks and through orifices, *Journal of Fluid Mechanics* 102 (1981) 279–299.

[24] J.E. Martin, E. Meiburg, Numerical investigation of three-dimensionally evolving jets subject to axisymmetric and azimuthal perturbations, *Journal of Fluid Mechanics* 230 (1991) 271–318.

[25] M. Nitsche, R. Krasny, A numerical study of vortex ring formation at the edge of a circular tube, *Journal of Fluid Mechanics* 276 (1994) 139–161.

[26] Sir H. Lamb, *Hydrodynamics*, Cambridge University Press, Cambridge, 1932, re-issued 1993.

[27] P.G. Saffman, *Vortex Dynamics*, Cambridge University Press, Cambridge, 1992.

[28] M. Abramowitz, I.A. Stegun, *Handbook of Mathematical Functions*, Dover Publications, New York, 1972.

[29] W.H. Press, S.A. Teukolsky, W.T. Vetterling, B.P. Flannery, *Numerical Recipes in FORTRAN. The Art of Scientific Computing*, second ed., Cambridge University Press, Cambridge, 1992.

[30] A.J. Majda, A.L. Bertozzi, *Vorticity and Incompressible Flow*, Cambridge University Press, Cambridge, 2002.

[31] G. Tryggvason, W.J.A. Dahm, K. Sbeih, Fine structure of vortex sheet rollup by viscous and inviscid simulation, *Journal of Fluids Engineering* 113 (1991) 31–36.

[32] M.S. Howe, *Theory of Vortex Sound*, Cambridge University Press, Cambridge, 2003.

[33] P.M. Morse, H. Feshbach, *Methods of Theoretical Physics—Part I*, McGraw-Hill, New York, 1953.

[34] D.G. Crighton, A.P. Dowling, J.E. Ffowcs Williams, M. Heckl, F.G. Leppington, *Modern Methods in Analytical Acoustics*, Springer, London, 1992.

[35] M.J. Lighthill, The Bakerian Lecture 1962. Sound generated aerodynamically, *Proceedings of the Royal Society of London A* 267 (1962) 147–182.

[36] P.M. Morse, K.U. Ingard, *Theoretical Acoustics*, Princeton University Press, Princeton, NJ, 1986.

[37] V.L. Wells, R.A. Renaut, Computing aerodynamically generated noise, *Annual Review of Fluid Mechanics* 29 (1997) 161–199.

[38] O.C. Zienkiewicz, Achievements and some unsolved problems with the finite element method, *International Journal of Numerical Methods in Engineering* 47 (2000) 9–28.

[39] H. Aref, Integrable chaotic and turbulent vortex motion in two-dimensional flows, *Annual Review of Fluid Mechanics* 15 (1983) 345–389.

[40] O. Inoue, Double-frequency forcing on spatially growing mixing layers, *Journal of Fluid Mechanics* 234 (1992) 553–581.

[41] D.G. Crighton, Acoustics as a branch of fluid mechanics, *Journal of Fluid Mechanics* 106 (1981) 261–298.

[42] C.-M. Ho, P. Huerre, Perturbed free shear layers, *Annual Review of Fluid Mechanics* 16 (1984) 365–424.

[43] L. Brevdo, A dynamical system approach to the absolute instability of spatially developing localized open flows and media, *Proceedings of the Royal Society of London A* 458 (2002) 1375–1397.

[44] Y. Otsuki, Y. Muroya, *Shin Sūgaku Kōshiki Shū II* (New Mathematical Formulae Collection, Vol. II. Japanese translation of original Russian text), Maruzen, Tokyo, 1991.